

UNIVERSITÀ
POLITECNICA
DELLE MARCHE

Dipartimento di Ingegneria Industriale e Scienze Matematiche
Corso di Laurea Magistrale in Ingegneria Meccanica

Wave and stress evolution during the nucleation of dynamic shear ruptures in laboratory earthquakes triggered by explosions

Analisi della propagazione d'onda e delle condizioni di sollecitazione nella fase di nucleazione di rotture di Modo II durante terremoti in scala

Advisor:
Prof. Marco Rossi, PhD

Co-advisor:
Dr. Attilio Lattanzi, PhD

Candidate:
Serena Pucci

Academic Year 2023-2024



UNIVERSITÀ
POLITECNICA
DELLE MARCHE

Dipartimento di Ingegneria Industriale e Scienze Matematiche
Corso di Laurea Magistrale in Ingegneria Meccanica

Wave and stress evolution during the nucleation of dynamic shear ruptures in laboratory earthquakes triggered by explosions

Analisi della propagazione d'onda e delle condizioni di sollecitazione nella fase di nucleazione di rotture di Modo II durante terremoti in scala

Advisor:
Prof. Marco Rossi, PhD

Co-advisor:
Dr. Attilio Lattanzi, PhD

Candidate:
Serena Pucci

Academic Year 2023-2024

Università Politecnica delle Marche
Dipartimento di Ingegneria Industriale e Scienze Matematiche
Corso di Laurea Magistrale in Ingegneria Meccanica
Via Brecce Bianche – 60131 Ancona (AN), Italy

A mio fratello Marco.

Ai miei genitori Monia e Andrea.

Abstract

It is important to understand the mechanisms that concern earthquakes generated by human activity. While usually the interest lays on the later stages of rupture propagation, it is noteworthy to focus the attention on the nucleation phase of a shear rupture, which can model earthquakes. A way to study the phenomenon is through scaled laboratory earthquakes, in which dynamic shear ruptures are generated through the sublimation of a wire embedded in the lower half of a PMMA plate, which has a certain interface angle and is loaded uniaxially. Through an experimental analysis, dilatational waves are traced with digital image correlation and the stress state at the interface is investigated during the nucleation of the shear rupture. It emerges that the nucleation phase is independent of interface angle and frictional properties. In addition, by means of a tridimensional finite element analysis, a spatio-temporal variation of the interface-normal stress is imposed using data obtained from the experiment to simulate the perturbation caused by the wire explosion. Outside the perturbed region, it appears that the finite element model partially simulates the rupture: the supershear rupture velocity is the same but the interface-parallel velocity peak is smaller. To capture the rupture behaviour in the perturbed region, the results suggest that a smaller but stronger perturbation is necessary. Ultimately, the tridimensional simulation reveals that there is slip in the direction perpendicular to the surface of the specimen.

Sommario esteso

Il presente lavoro si concentra sull'analisi della fase di nucleazione di rotture di modo II, con particolare attenzione alla propagazione d'onda e allo stato di sollecitazione derivanti dalla sublimazione di un cavo in Ni-Cr, costituente l'innesco della rottura stessa.

Si tratta di uno studio sia sperimentale che numerico, la cui base teorica è fondata su elastodinamica, modelli di attrito rate-and-state e in parte meccanica della frattura. Dal punto di vista sperimentale, il setup utilizzato fa parte del laboratorio del prof. Ares J. Rosakis presso il California Institute of Technology e l'idea che vi è alla base è quella di produrre una sollecitazione normale e di taglio su un'interfaccia tra due superfici che si scambiano forze di attrito. Attraverso la sublimazione di un cavo in Ni-Cr, si va a perturbare la tensione normale all'interfaccia causando una momentanea riduzione dello sforzo tangenziale di attrito che bilancia la tensione tangenziale imposta all'interfaccia, causando scorrimento e conseguente innesco della rottura di modo II. Per ottenere quanto appena riportato, si utilizza una piastra rettangolare in polimetilmetacrilato di dimensioni 200 mm $\times$ 250 mm $\times$ 12.5 mm che viene tagliata attraverso una macchina CNC in due parti uguali non più rettangolari ma quadrilaterali, con un lato inclinato di un angolo α. Il provino viene sottoposto a compressione monoassiale con una pressa idraulica ed è proprio la combinazione di tale sollecitazione globale con l'inclinazione α dell'interfaccia che permette di ottenere, sull'interfaccia stessa, lo stato tensionale desiderato.

Gli obiettivi principali sono la misura della velocità delle onde dilatazionali causate dalla sublimazione del cavo, nonché la visualizzazione delle suddette onde attraverso la digital image correlation (DIC), quando finora sono sate osservate soltanto con la fotoelasticità. A questi, segue uno studio della perturbazione dello stato tensionale e di come l'inclinazione α e le proprietà di attrito dell'interfaccia influenzano la nucleazione stessa. Di altrettanta importanza è la simulazione numerica della fase iniziale dell'esperimento, in quanto sinora l'interesse nel simulare questa tipologia di esperimenti era rivolto principalmente alla fase di propagazione di tali rotture. L'argomento trattato è di particolare rilevanza nel campo della geofisica, in cui lo studio di questa tipologia di rotture consente una comprensione più approfondita del fenomeno dei terremoti ma un aspetto particolarmente interessante è comunque la totale generalità delle leggi che governano il fenomeno studiato.

Come indicato in precedenza, l'analisi delle deformazioni che interessano il provino viene fatta con l'aiuto della digital image correlation bidimensionale: le immagini sono catturate a 5 milioni di frame al secondo tramite una telecamera ad alta velocità e il field of view di 30 mm $\times$ 20 mm è posto a circa 2 mm dal punto in cui vi è il cavo in Ni-Cr. In aggiunta, sono stati utilizzati due velocimetri laser per ottenere la componente della velocità parallela all'interfaccia in due punti a distanza di 10 mm e 22 mm dall'intaglio che alloggia il cavo in Ni-Cr, punti che appartengono alla piastra superiore e si trovano a distanza nulla dall'interfaccia.

Per quanto riguarda il lato numerico, l'esperimento è stato simulato tridimensionalmente con il codice agli elementi finiti PyLith che permette di utilizzare la formulazione rate-and-state dell'attrito come legge costitutiva dell'interfaccia. Il time-stepping temporale è di tipo esplicito e la mesh è tetraedrica. Si impone la condizione iniziale dell'interfaccia attraverso la sua velocità di scorrimento iniziale, che dipende dal tempo trascorso dal momento in cui le due superfici dell'interfaccia sono entrate in contatto, e si simula la sublimazione del

cavo in Ni-Cr come una variazione spazio-temporale della tensione normale all'interfaccia.

Analizzando i risultati sperimentali, emerge come il fronta dell'onda dilatazionale emessa dall'esplosione del cavo sia visualizzabile nella traccia del tensore velocità di deformazione, che rappresenta la velocità di variazione del volume ed è pertanto una grandezza particolarmente sensibile a onde di tipo dilatazionale; quanto osservato è coerente con il fronte d'onda calcolato utilizzando la velocità delle onde dilatazionali ottenuta dalle misure dei velocimetri laser. Si studia poi la durata e l'estensione della perturbazione della tensione normale all'interfaccia ed emerge infine come, seppure la meccanica della frattura abbia contribuito ad importanti avanzamenti nello studio di questa tipologia di rotture, l'attrito è un aspetto assolutamente non trascurabile nel determinare le caratteristiche della rottura che si va a generare in una determinata interfaccia. Per ciò che concerne la simulazione numerica, c'è una buona fedeltà dei risultati numerici con quelli sperimentali al di fuori della regione perturbata: la velocità di propagazione della rottura supershear è circa la stessa di quella ottenuta dagli esperimenti anche se i picchi di velocità parallela all'interfaccia sono di intensità minore. Inoltre, la transizione al regime supershear avviene in un punto più lontano rispetto al caso sperimentale. Infine, l'analisi tridimensionale consente di studiare anche la componente dello spostamento al di fuori del piano del provino su cui si effettua l'analisi DIC: si riscontra la presenza di scorrimento anche in tale direzione, attribuibile ad alle onde di taglio in quanto si osserva antisimmetria rispetto a due piani: il piano perpendicolare alla superficie del campione e contenente l'intaglio per il cavo e il piano parallelo alla superficie del campione che si trova a metà del suo spessore. Lo scorrimento avviene quindi in direzione opposta sulla superficie anteriore e posteriore del campione. In conclusione, mentre dal lato sperimentale lo studio può considerarsi conclusivo, dal lato numerico è possibile un'ulteriore approfondimento attraverso, ad esempio, l'utilizzo di un modello costitutivo viscoelastico, valutandone gli effetti che ne conseguono rispetto ad un semplice modello lineare elastico.

Contents

1 Introduction **1**

2 Theoretical foundation **3**

2.1 Elastodynamics 3

2.2 Friction 6

2.2.1 Rate-and-state friction 7

2.2.2 State variable evolution laws 9

2.2.3 Flash heating 10

2.3 Shear ruptures 11

2.3.1 Sub-Rayleigh and supershear ruptures 13

2.3.2 Nucleation of shear ruptures 14

3 Materials and methods **18**

3.1 Specimen 18

3.1.1 Interface surface preparation 19

3.1.2 Speckle pattern 21

3.2 Experimental setup 21

3.2.1 Heterodyne laser velocimetry 25

3.2.2 Laser velocimeters support system 25

3.2.3 Reflective tapes 26

3.3 Test procedure 27

3.4 Digital Image Correlation 30

3.5 Data processing 32
3.5.1 Filtering of oscilloscope data 32
3.5.2 DIC Post-processing 33
3.6 Experiments 33
3.7 Finite element simulation 34
3.7.1 Boundary and initial conditions 37
3.7.2 Simulation of the nucleation process 38

4 Results and Discussion **39**
4.1 P-wave speed 40
4.2 P-wave front 43
4.3 Stress state 46
4.4 Independence of nucleation properties from friction and interface angle 50
4.5 Supershear and sub-Rayleigh rupture: the importance of friction 52
4.6 FE simulation 55
4.6.1 Influence of nucleation parameters 56
4.6.2 Out-of-plane slip and velocity 56
4.6.3 DIC - FE comparison 59

5 Conclusion **66**

Bibliography **68**

Acknowledgments **71**

Ringraziamenti **73**

List of Figures

2.1 Displacement field associated with longitudinal waves (a) and transverse waves (b) [1]. 5
2.2 Schematic representation of Rayleigh waves [1]. 6
2.3 Linear slip-weakening friction law. 7
2.4 Rate-and-state friction law: velocity jump experiment. 9
2.5 Schematic image showing mode I, mode II and mode II fractures with the corresponding stress field [9]. 12
2.6 Sub-Rayleigh and supershear ruptures captured with photoelasticity [12]. 14
2.7 Stick-slip model (a) and corresponding relation between frictional force, elastic force and slip [8]. 15
2.8 Slipping region as a function of time and space [8]. 16

3.1 Specimen geometry. 20
3.2 Bead-blasting. 20
3.3 Example of speckle pattern. 21
3.4 Experimental setup scheme. 23
3.5 Experimental setup. 24
3.6 Laser velocimeters setup. 26
3.7 Laser beams and reflective tapes scheme. Tape corner coordinates are in millimeters. 27
3.8 Specimen holder. 28
3.9 Specimen setup right before the wire explosion. 30

3.10 Field of view. 31
3.11 Debris from the explosion, especially visible in one of the experiments. 32
3.12 Cohesive cells used in the fault implementation [21]. 35
3.13 Influence of the number of mesh elements on the interface-parallel velocity. 36
3.14 Detail of the tetrahedral mesh. 36
3.15 Spatio-temporal variation of the interface-normal stress to simulate the Ni-Cr wire sublimation. 38

4.1 Interface-parallel velocity obtained from the laser velocimeters with P-wave and S-wave arrival times for $\alpha = 28°$ (test 1). . . . 41
4.2 Two independent measures obtained with the laser velocimeters positioned at 10 mm from the nucleation site for a specimen with $\alpha = 28°$. 42
4.3 Comparison of the interface-parallel velocity obtained through DIC and laser velocimeters for $\alpha = 28°$. 43
4.4 Volumetric strain rate field showing the propagation of the P-wave front for $\alpha = 24°$ (a) and $\alpha = 28°$ (b). 45
4.5 Interface-normal stress as a function of time, for a point on the lower plate. 46
4.6 Interface-normal stress along the interface on the upper (a) and lower (b) plate at $t = 9$ µs for an angle $\alpha = 24°$. 48
4.7 Shear stress as a function of time, for a point on the lower plate. 48
4.8 Shear stress and slip rate as a function of time for the specimen with $\alpha = 24°$, obtained through DIC. 49
4.9 Slip rate at $x_1 = 10$ mm (a) and $x_1 = 25$ mm (b) for tests with different interface angle and holding time. 51
4.10 Colormaps showing full-field measures of interface-parallel velocity, interface-normal velocity and shear strain for two experiments conducted on the same specimen with $\alpha = 28°$. 53

4.11 Slip rate as a function of time and space. 54
4.12 Effect of $\Delta\sigma$ on the interface-parallel velocity. 56
4.13 Out-of-plane slip for two points located at the same distance from the nucleation site but on opposite sides of the specimen. . 57
4.14 Out-of-plane slip field on the interface at two different time instants. 57
4.15 Out-of-plane velocity field at two different time instants on the front (a) and back (b) of the specimen. 58
4.16 Comparison between FE and DIC data of the slip rate at different distances from the nucleation size a 60
4.17 Interface-parallel velocity at different distances from the nucleation site: $|x_1| \leq D/2$ (a) and $|x_1| > D/2$ (b). FE simulation results are compared with experimental data. 61
4.18 Slip rate comparison between experiment (a) and FE simulation (b). 62
4.19 Effect of a smaller D on the P-wave velocity peak in the interface-parallel velocity. 63
4.20 Interface-parallel (a) and interface-normal (b) velocity field at two different time instants. 65

List of Tables

3.1 Experiments conducted. 33

4.1 Simulated nucleation parameters. 55

Chapter 1

Introduction

The work presented here aims to analyze the nucleation phase of dynamic shear ruptures triggered by explosions, both experimentally and numerically. The interest in the initial phase of this type of experiment is important in light of the fact that usually the focus is on the later stages of rupture propagation rather than its initiation, both in experiments and in simulations. Moreover, it is a topic of notable importance in the geophysics community due to the fact that this kind of ruptures can model earthquakes, even if the laws that govern the phenomenon are utterly general. Since the shear ruptures in the experiments are triggered by explosion, this work is particularly relevant for earthquakes induced by human activities.

A way to simulate earthquakes is through scaled experiments where the material used is brittle as rocks but has a significantly smaller shear modulus. This allows ruptures to nucleate on a much smaller scale: millimeters instead of kilometers. The experimental setup used to induce such ruptures is part of the laboratory equipment at the California Institute of Technology and is one of the few laboratories of its kind. Through an hydraulic press, a specimen made of two plates with a certain interface angle is loaded uniaxially; the presence of the interface is a key factor in the sense that it allows to load the interface with

a certain combination of shear and normal stress, simulating tectonic stress. The rupture is then triggered through the explosion of a wire embedded in the lower plate, which weakens the shear resistance of the interface.

In particular, from the experimental point of view one of the main objectives is tracing the dilatational waves originating from the explosion with digital image correlation, considering that they were usually identified by means of photoelasticity. Additionally, it is important to understand how the stress state at the interface is perturbed by the explosion, mainly in terms of interface-normal stress. Additionally, interface-parallel particle velocity obtained through laser velocimeters is used to calculate the dilatational wave speed. From the numerical point of view, it is noteworthy to investigate if the nucleation process can be simulated by means of the finite element code PyLith, which has the advantage of implementing a rate-and-state friction formulation to model the interface behaviour; a tridimensional simulation allows also to explore the out-of-plane slip and velocity that are associated with a shear rupture.

Beginning with the theoretical foundation this study is based on, the second chapter delves into elastodynamics, friction formulations and shear ruptures. Afterwards, the materials and methods employed in this work are presented in the third chapter, with a focus on the specimen, the material used, the experimental setup and the parameters concerning the numerical simulation. In the fourth chapter, the experimental and numerical results are discussed.

Chapter 2

Theoretical foundation

The material discussed in this chapter represents the theoretical foundation on which this work is based, focusing on elastodynamics, frictional behavior and shear ruptures. Starting from the waves that can propagate in an elastic solid medium, the attention is then shifted to friction formulations that differ from the traditional rate-and-state independent model that is the Coulomb friction model. This is particularly important because shear ruptures propagate on weakness planes which are, in fact, frictional interfaces. Finally, the theory behind shear ruptures is outlined in order to understand the mechanisms involved, which types of rupture exist and the way they nucleate.

2.1 Elastodynamics

Crucial in this work is the understanding of the kind of waves that can propagate in a medium or in one of its surfaces due to their strong correlation with shear ruptures.

Starting from the body waves, the governing equation for an elastic medium can be derived expanding in Taylor series the equation of motion (Equation (2.1))

with respect to the strain $\boldsymbol{\epsilon} = \nabla\boldsymbol{\xi}(\mathbf{x}, t)$ [1], where $\boldsymbol{\xi}(\mathbf{x}, t)$ is the displacement vector. This can be done assuming that that the solid remains in the elastic regime, which involves small displacements.

$$\frac{\partial \rho}{\partial t} = \nabla \cdot (\rho \mathbf{v}(\mathbf{x},\ \mathbf{t})) = 0 \tag{2.1}$$

A solution can be found in the form of a monochromatic plane-wave, that is a single-frequency wave which has constant amplitude and frequency on any plane perpendicular to the direction of propagation $\hat{\mathbf{k}}$.

The quantity that oscillates, $\boldsymbol{\xi}(\mathbf{x}, t)$, can be resolved into the sum of two components, one along $\hat{\mathbf{k}}$ and the other one perpendicular to $\hat{\mathbf{k}}$:

$$\boldsymbol{\xi} = \boldsymbol{\xi}_L + \boldsymbol{\xi}_T \tag{2.2}$$

As shown in Figure 2.1a, $\boldsymbol{\xi}_L$ represents the longitudinal component of the wave and it induces displacement in the same direction of the propagation; its divergence is non-zero, meaning that the vector field causes expansion, while its curl is nil. Since longitudinal waves are associated with expansion and therefore change in volume, they are also called dilatational waves and in seismology P-waves.

Instead, $\boldsymbol{\xi}_T$ is the transverse or shear component, which has zero divergence but non-zero curl. It features displacements perpendicular to the direction of propagation (Figure 2.1b) and, given that they are driven by shear stress, they do not exist in fluids but only in solids. In seismology, they are called S-waves.

For an elastic medium, the analysis mentioned above leads to the relations between the P-wave speed c_s, the S-wave speed c_s, the Young modulus E, the shear modulus G and the Poisson ratio ν:

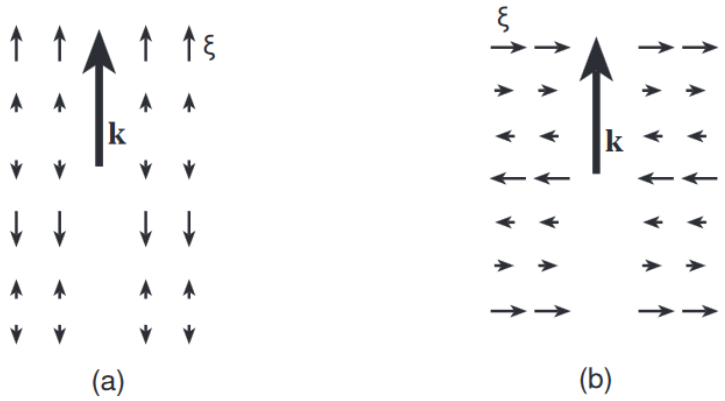


Figure 2.1: Displacement field associated with longitudinal waves (a) and transverse waves (b) [1].

$$c_p = \sqrt{\frac{E(1-\nu)}{\rho(1+\nu)(1-2\nu)}} \tag{2.3}$$

$$c_s = \sqrt{\frac{G}{\rho}} = \sqrt{\frac{E}{2\rho(1+\nu)}} \tag{2.4}$$

The P-wave speed is higher than the S-wave speed.

In addition to body waves, another phenomenon is that of edge waves, which have the distinctive feature of propagating on a discontinuity and are mainly relevant in seismology. A particular type of edge waves are surface waves: they propagate on the surface of a medium and decrease exponentially with depth. The simplest example of surface waves is Rayleigh waves , which are an intertwined mixture of P and S waves [1]; in fact, the displacements they induce are both longitudinal and transverse (Figure 2.2). The Rayleigh wave speed c_R is typically $87-95\%$ of the shear wave speed for an isotropic linear elastic medium [2].

This type of waves are relevant to this study because c_R together with c_s and c_p identify three rupture velocity regimes that will be discussed in Section 2.3. Depending on which regime the rupture (i.e. earthquakes) falls into, the displacement and stress field will be different around the rupture tip.

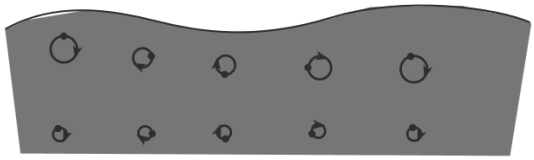


Figure 2.2: Schematic representation of Rayleigh waves [1].

2.2 Friction

In order to understand how shear ruptures nucleate first ad then propagate, it is crucial to further explore friction and, specifically, it is important to consider a model that takes into account the slip rate V, namely the relative sliding velocity between the two surfaces in contact at an interface.

The Coulomb friction model (Equations (2.5) and (2.6)) is not optimal. In fact, even if it states that there is a difference between static and dynamic friction, slip happens instantaneously if the friction coefficient $f = \frac{\text{shear stress}}{\text{normal stress}}$ overcomes the static friction f_s and f remains constant as the slip δ increases. Moreover and most importantly, there is no dependence on the slip rate V.

$$F_t \leq f_s F_n \quad \text{and} \quad \delta = 0 \tag{2.5}$$

$$F_t = f_d F_n \quad \text{and} \quad \delta \neq 0 \tag{2.6}$$

Another model that is frequently used is the linear slip-weakening friction (Equation (2.7) and Figure 2.3), according to which, as slip increases, the friction coefficient decreases from a static value f_s to a lower dynamic value f_d as slip progresses along the frictional interface. When the slip reaches a characteristic slip distance D_c, the friction stops decreasing and remains constant over time.

$$f = \begin{cases} f_s - (f_s - f_d)\frac{\delta}{D_c} & \text{if } \delta \leq D_c \\ f_d & \text{if } \delta > D_c \end{cases} \tag{2.7}$$

It is a formulation that is still used both in numerical simulations and theoretical analysis, but it is evident how it fails to capture the way the frictional properties of an interface change for different slip rate histories [3]. In fact, experiments with different far-field loads show not only that f_d and D_c are not material properties since they change, but they also show how the relation between friction and slip is substantially different in these experiments, making it clear that slip rate is not a negligible aspect when modeling and studying the frictional interaction between two surfaces [3].

In conclusion, even if it models the frictional weakening that is necessary for a shear rupture to nucleate and propagate, a purely slip-dependent friction law does not reflect the true nature of friction and a model that takes into account the effect of slip rate is necessary.

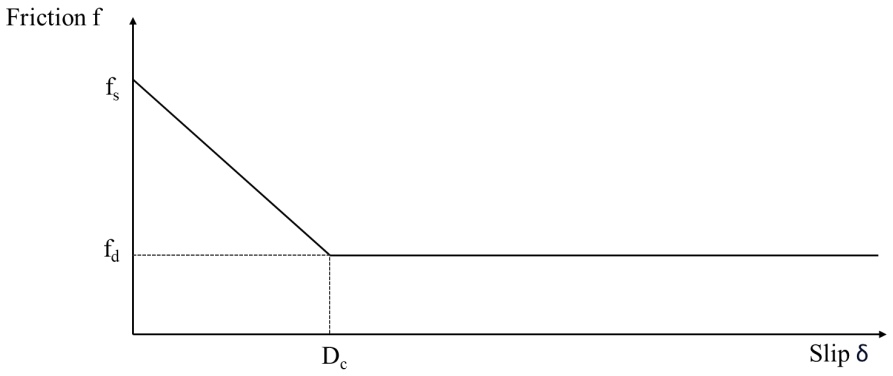


Figure 2.3: Linear slip-weakening friction law.

2.2.1 Rate-and-state friction

Rate-and-state dependent friction was first introduced in the late 1970s and early 1980s by Dietrich [4] and Ruina [5] and it is characterized by a system of first-order algebraic-differential equations: Equation (2.8) and an evolution law

for the state variable. It is based on the assumption that a surface has a state θ at any instant in time that reflects its slip history; additionally, friction is a function of state and slip rate V, while the rate of change of θ depends on θ itself and V. In terms of dimensional analysis, θ is measured in seconds.

$$f(V,\theta) = f^* + a \ln \frac{V(t)}{V^*} + b \ln \frac{V^*\theta(t)}{D_{RS}} \tag{2.8}$$

If we look at Equation (2.8), we see that there are three terms:

- f^* is the friction measured at a reference slip rate V^*;
- $a \ln \frac{V(t)}{V^*}$ accounts for a rate dependency of the frictional strength during the onset of slip (Figure 2.4), often referred as "direct effect", and it relates to the asperities that break when there is relative motion between the two surfaces in contact [6]. a is here a constant that depends on the frictional properties of the interface;
- $b \ln \frac{V^*\theta(t)}{D_{RS}}$ is associated with the frictional weakening of the interface, which is defined as the healing effect, and can be interpreted as the growing effective contact area [6]. b is a constant that depends on the frictional properties of the interface.

The constant D_{RS} represents the sliding distance over which f decreases to a lower friction coefficient due to the healing effect. The value of friction that is reached due to the healing effect depends logarithmically on the slip rate.

Since Equation (2.8) is an empirical formulation, it is important to mention that it is difficult to define a precise and certain physical meaning, even if, to a certain extent and as mentioned above, a physical interpretation is still possible.

A significant difference with the traditional Coulomb friction model is that a rate-and-state formulation does not admit zero slip if there is shear stress

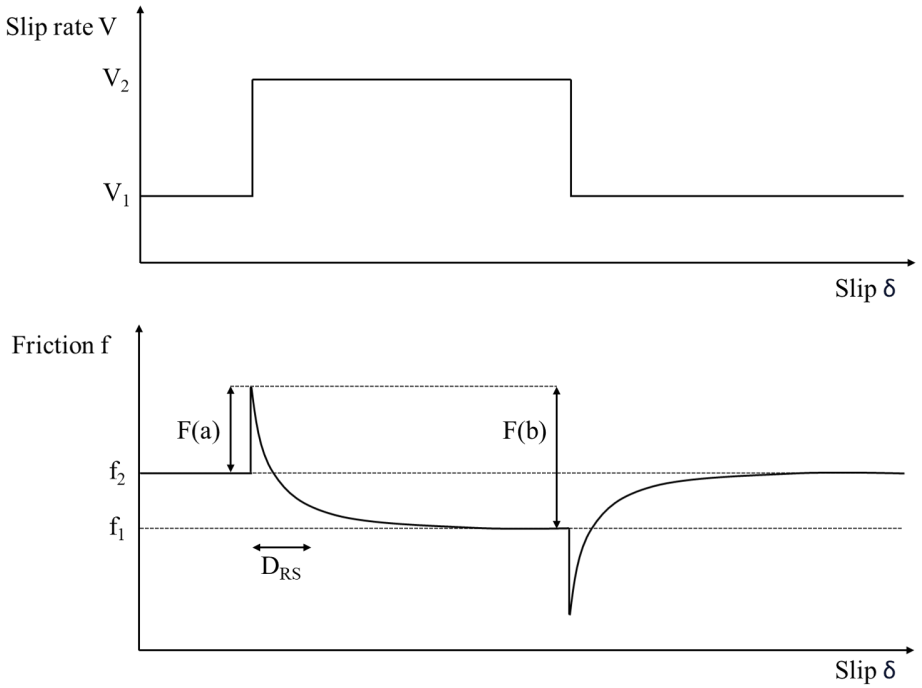


Figure 2.4: Rate-and-state friction law: velocity jump experiment.

acting on the interface surface. This is backed up by experimental evidence [6]: even for an extended amount of time (up to two weeks), a non-zero slip is still measured in tests that aim to replicate a block on an inclined plane, with an inclination angle that is far from the value that would cause the transition from the static regime to the dynamic regime according to the Coulomb friction model. The slip rate keeps decreasing with time and, although extremely small, it is never zero. Since these tests are designed to maintain the stress state at the interface constant, thus meaning that f is constant too, the change in slip rate is caused by a variation in θ: as V decreases, θ increases. This type of experiments allows to obtain the so-called healing curves, which describe the relation between slip rate and time during the interface healing [7].

2.2.2 State variable evolution laws

As previously mentioned, Equation (2.8) has to be coupled with an evolution law for the state variable. Which is the best equation to be used is still up for

debate. The most widely used equations are the following:

$$\frac{d\theta}{dt} = 1 - \frac{V(t)\theta(t)}{D_{RS}} \tag{2.9}$$

$$\frac{d\theta}{dt} = -\frac{V(t)\theta(t)}{D_{RS}} \ln \frac{V(t)\theta(t)}{D_{RS}} \tag{2.10}$$

Equation (2.9) is the "aging law": it was first introduced by Dietrich and it asserts that, even if $V = 0$, θ increases with time, which represents the healing of the interface surface. Equation (2.10) is the "slip law", it was first proposed by Ruina and unlike the "aging law", a change in the state of the interface is possible only if the slip rate is non-zero.

For both evolution laws, when $\frac{d\theta}{dt} = 0$ at steady state, $\theta = \frac{D_{RS}}{V}$ is the time that has passed since the surfaces came into contact [6]. At steady state, the friction coefficient is:

$$f_{\text{steady state}} = f^* + (a - b) \ln \frac{V}{V^*} \tag{2.11}$$

It is worthy to note that if $a < b$, the interface is defined as velocity-weakening since the steady state friction coefficient decreases with the slip rate. Instead, if $a > b$ the interface is velocity strengthening and $f_{\text{steady state}}$ increases with V.

2.2.3 Flash heating

In addition to the rate-and-state formulation discussed earlier, it is possible to include in the friction model a dynamic mechanism called flash heating, which refers to the frictional weakening that happens due to the surface asperities heating up when in contact and subjected to shear stress at high levels of slip rate [3]. The consequent friction coefficient can be defined with Equation (2.12).

$$f(V,\theta) = f_w + [f_{RS}(V,\theta) - f_w]\,\frac{V_w}{V} \tag{2.12}$$

In particular, f_{RS} represents the rate-and-state dependent friction showed in Equation (2.8), V_w indicates the value of slip rate for which the flash heating effect becomes non-negligible and f_w is the residual friction coefficient caused by flash heating. It is worth highlighting that for $V \to \infty$, $f \to f_w$ and that friction approaches its flash heating weakened value with a $1/V$ dependence on slip rate.

It is found that combining rate-and-state friction with the flash-heating formulation allows to have consistency in experimental data in terms of the relation between friction and slip rate [3].

2.3 Shear ruptures

The initial approach to studying shear ruptures was based on linear elastic fracture mechanic, which is a continuum mechanism approach that idealizes the crack as a mathematically narrow and flat slit in a linear elastic medium [8]. Analyzing the stress field around the crack, it is possible to correlate it to the applied stress, thus obtaining a relation between macroscopic and intrinsic strength of the material.

Shear ruptures were then treated as if they were mode II fractures: this particular fracture mode is caused by in-plane shear stresses and the corresponding displacements occur in the direction perpendicular to the crack edge and in the plane of the crack (Figure 2.5).

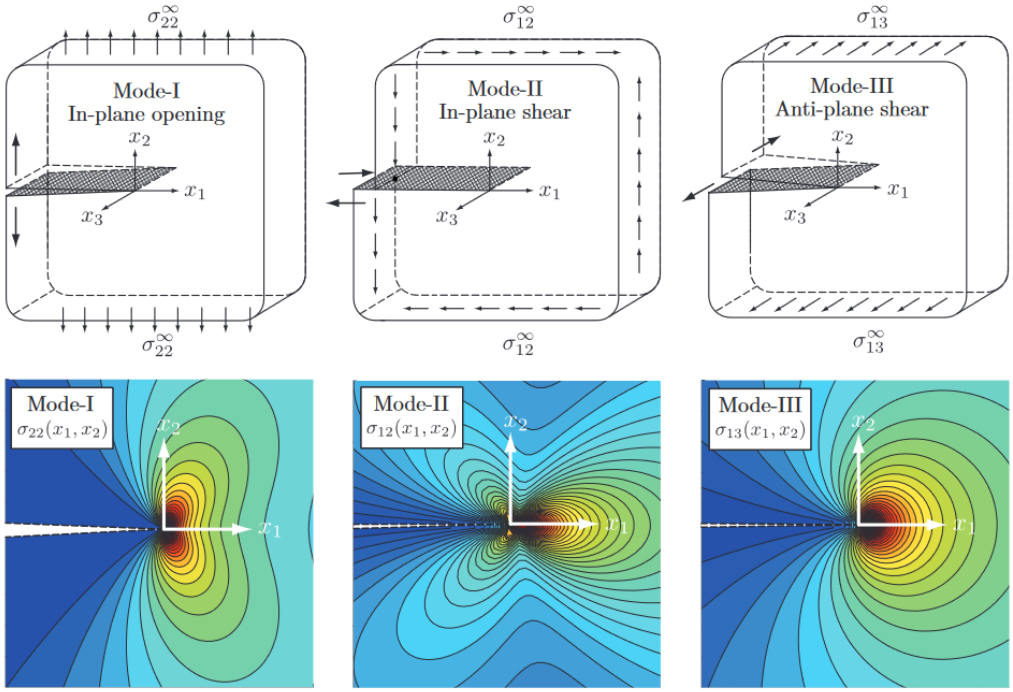


Figure 2.5: Schematic image showing mode I, mode II and mode II fractures with the corresponding stress field [9].

Nevertheless, it became clear how shear ruptures are not exactly mode II fractures. Firstly, shear ruptures propagate only on a weak path and secondly, fracture mechanics completely disregards the contribution of friction, assuming the crack to be cohesionless behind the crack tip [8]. In terms of energy balance, the work against friction is not negligible.

The propagating rupture, namely a displacement discontinuity, acts as a continuous source of dilatational and shear waves and the rupture velocity V_R is defined as the speed of the moving boundary between the regions where there is slip and those where the slip is still zero ahead of the rupture tip.

The investigation of this type of rupture is relevant for any of those solid materials that contain weak fracture paths: even if there is homogeneity in its constitutive properties, there is inhomogeneity in its toughness and fracture resistance. This applies not only to common engineering materials but also, on another scale, to earthquake's faults.

2.3.1 Sub-Rayleigh and supershear ruptures

A shear rupture can be categorized based on the speed of its propagating front. Specifically, three regimes can be identified by the characteristic velocities of the material: $c_R < c_s < c_p$.

Initially, it was thought impossible to have supershear ruptures because if the steady-state rupture velocity falls between the Rayleigh wave speed and the shear wave speed, the energy at the rupture tip is negative, which means that energy is there produced. This leads to exclude the possibility of steady-state crack growth in that specific speed interval but it doesn't eliminate the option of the rupture discontinuously and transiently go from one rupture speed to another [2]. In fact, even if the majority of earthquakes are sub-Rayleigh, i.e. the rupture velocity equals 80% of the shear wave speed [10], there is now evidence of supershear earthquakes.

The transition from sub-Rayleigh to supershear happens through the Burridge-Andrews mechanism. It is found that a peak in shear stress propagates ahead of the rupture tip; this peak increases progressively as V_R nears the Rayleigh wave speed and if it exceeds the static frictional limit, it can lead to the formation of a secondary microrupture, the so-called daughter crack, ahead of the main rupture. If the interface is strong enough, the main rupture keeps propagating at c_R, otherwise it joins the secondary rupture and acquires a speed that is higher than the shear wave speed and close to the dilatational wave speed [11, 12].

When the rupture is in the intersonic regime ($c_s < V_R < c_p$) the nature of the governing differential equations changes profoundly: if we consider two-dimensional plane elastodynamics at steady-state, for $V_R < c_R$ both governing equations are elliptic while in the intersonic regime one equation is elliptic and the other is hyperbolic. In the same way as an object moving through air at a speed higher than the speed of sound (i.e. the speed of dilatational waves), this

implies the presence of a Mach cone or Mach lines originating from the crack tip (Figure 2.6). These characteristic lines are related to shear deformations and they appear in the form of spatial discontinuities.

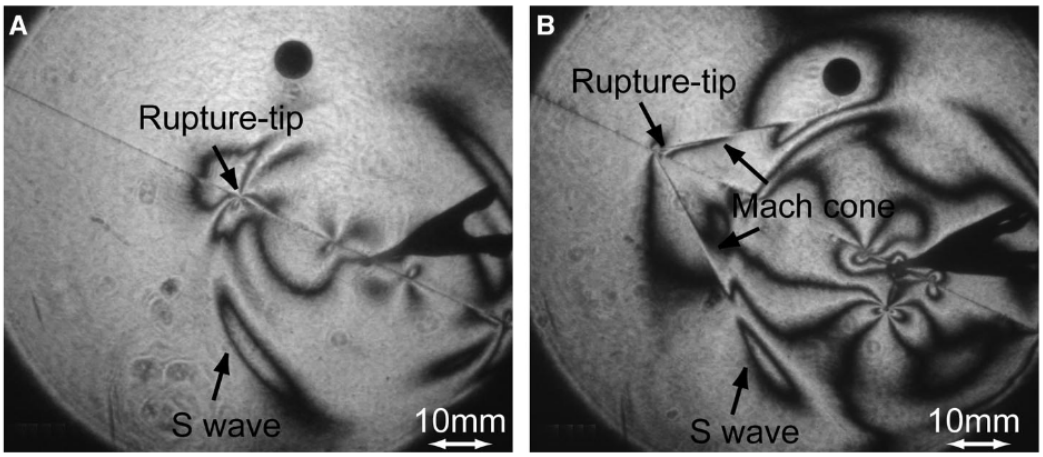


Figure 2.6: Sub-Rayleigh and supershear ruptures captured with photoelasticity [12].

2.3.2 Nucleation of shear ruptures

Considering that friction experiments suggest that earthquakes might be equivalent to stick-slip instabilities [5], a fault can be modeled as a block which can slide on a surface and is loaded with a spring (Figure 2.7a). The interface between the block and the surface is subjected to friction and is analogous to the fault, while the stiffness K of the spring may represent the elastic medium that surrounds it [8]. This is also the reason behind the rate-and-state friction formulation and the velocity jump experiments mentioned above.

In this kind of system, a sudden increase in slip along with a drop in stress can happen due to dynamic instability: if there is a change in the frictional force, the elastic medium might not respond as fast as the frictional force changes, causing a force imbalance that results in the acceleration of the system. As shown in Figure 2.7b, from equilibrium point B, the system rapidly shifts to point C, after which the frictional force becomes greater than the elastic force

and the system halts at point D until a new dynamic instability occurs.

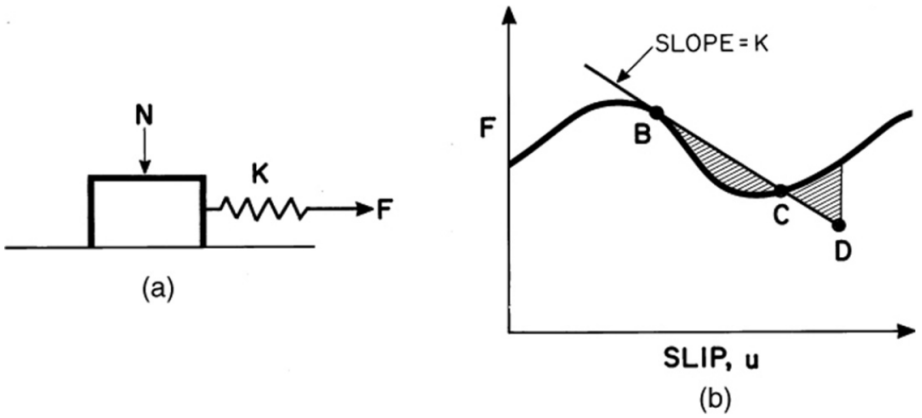


Figure 2.7: Stick-slip model (a) and corresponding relation between frictional force, elastic force and slip [8].

What is depicted in Figure 2.7b is essentially a slip-weakening system, which does not explain exactly how friction will go back to its initial value and eventually oscillate around a mean value in stick-slip phenomena that can model earthquakes. This is why rate-and-state friction is so important: it allows to model the healing of the interface, which progressively becomes stronger with time meaning that, after an instability event, the friction goes back to its static value; at the same time, if the formulation is velocity-weakening, it will eventually reach a state of regular stick-slip. On the contrary, if it is velocity strengthening, dynamic instabilities can occur, but they do not result in oscillations around a mean value and the unstable sliding rapidly ceases and the system returns to its state of stable sliding [8].

If we consider a velocity-weakening rate-and-state formulation, mathematically this translates to the presence of a Hopf bifurcation: if a parameter changes, the system fixed point is now unstable and oscillations arise. In particular, earthquakes nucleate only in the unstable regime and instability is reached when the slipping region reaches a critical length L_c or h^*. When h^* is reached, the rupture propagates dynamically (Figure 2.8).

Since the stability of the system depends on its stiffness, on the interface-

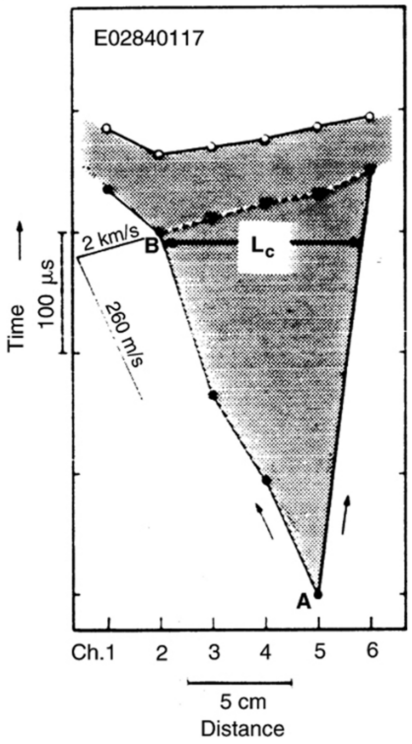


Figure 2.8: Slipping region as a function of time and space [8].

normal stress σ_n and on the frictional parameters a, b, and D_{RS}, it is possible to correlate h^* with these parameters. The way earthquake nucleation is modeled depends on the state variable evolution law: well above steady state, if the "aging law" is considered, the nucleation zone has a fixed length as slip accelerates; meanwhile, if the "slip law" is considered, the nucleation zone is smaller and its length decreases as slip accelerates [13]. Approaching steady-state, the nucleation zone increases in both cases.

Considering the "aging law", two distinct regimes can be identified depending on a/b [14]. For $a/b \gtrsim 0.5$ the slipping patch asymptotically reaches the value reported in Equation (2.13) [14], which derives from an energy balance.

$$h^* = \frac{[b(b-a)]^2}{\pi} \frac{G' D_{RS}}{b\sigma_n} \tag{2.13}$$

where $G' = G/(1-\nu)$ and G is the shear modulus. It is worth mentioning that

the nucleation length is consequently proportional to the shear modulus of the elastic medium.

For smaller a/b ratios and when healing is negligible ($V\theta/D_{RS} \gg 1$), the nucleation length is:

$$h^* = 2 \cdot 1.3774 \frac{G' D_{RS}}{b\sigma_n} \tag{2.14}$$

Chapter 3

Materials and methods

This chapter describes the materials and methods used to investigate the nucleation phase of shear ruptures. Starting from the material properties and geometry of the specimen, the experimental setup is presented and described. Afterwards, the testing procedure is detailed and the parameters used in the digital image correlation are mentioned. Lastly, the finite element simulation of the experiment is addressed.

3.1 Specimen

Figure 3.1 shows the geometry of the specimen used in the conducted experiments. The material is a polymethyl methacrylate (PMMA), which is a transparent amorphous thermoplastic polymer that has been used as correspondent to rocks, since it is still brittle but it has a shear modulus that is 25 times smaller than that of rocks, which allows to nucleate dynamic ruptures in much smaller scales (millimeters instead of kilometers) [6]. A rectangular PMMA plate, manufactured by Reynolds Polymer Technology, is cut by means of a CNC machine into two equal parts with an inclination angle α. Afterwards, a through-thickness notch is created in one of the two plates in order to

accommodate the wire that causes the explosion.

Considering a linear elastic constitutive model, PMMA material properties are the following:

- Density: $\rho = 1180$ kg/m^3
- Young modulus: $E = 5900$ MPa
- Poisson ratio: $\nu = 0.35$

Alternatively, instead of E or ν, one can define the properties of PMMA using the P-wave speed and the S-wave speed:

- P-wave speed: $c_p = 2.83$ km/s
- S-wave speed: $c_s = 1.37$ km/s

It is important to note that, given the viscoelastic nature of PMMA, the reported parameters refer to high strain rate levels since that is the strain rate regime that characterizes the rupture [15].

3.1.1 Interface surface preparation

The interface surface is first polished with a solution composed of water and cerium oxide (2:1) to remove possible imperfections arisen during machining. Once polished, it undergoes bead-blasting (Figure 3.2a, Figure 3.2b) for 3 minutes with McMaster-Carr abrasive glass beads of size $104 - 211$ µm, in order to obtain a controlled roughness level. Just before testing, the surface of the specimen is bead-blasted for 30 seconds to restore its frictional properties. During this whole process, the lateral surfaces of the specimen are protected using tape.

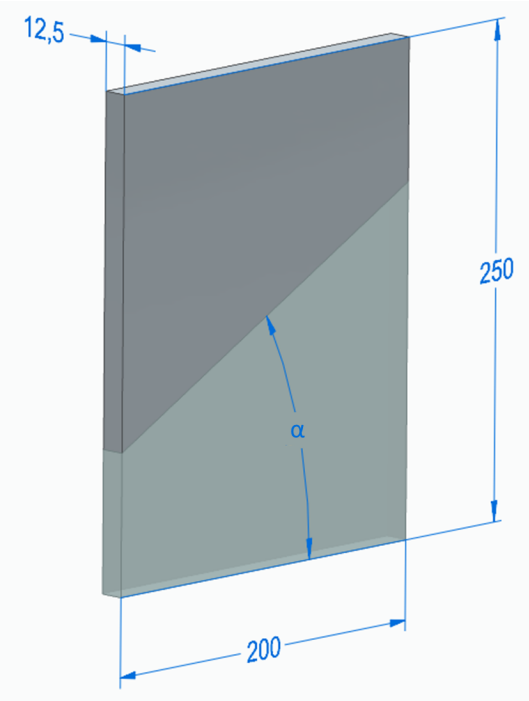


Figure 3.1: Specimen geometry.



(a) Bead-blasting cabinet



(b) Specimen in the bead-blasting cabinet

Figure 3.2: Bead-blasting.

3.1.2 Speckle pattern

To create the speckle pattern necessary for the digital image correlation (DIC), a layer of white paint is first sprayed on the specimen surface. Afterwards, a marker is used to manually create the dots. Its tip size allows to obtain a pattern with large dense dots (Figure 3.3), optimal for ultrahigh-speed DIC with a field of view of intermediate dimensions [16], as in our case. Contrary to a speckle pattern obtained with black spray paint, it allows to control the speckle size, thus reducing the error [16].

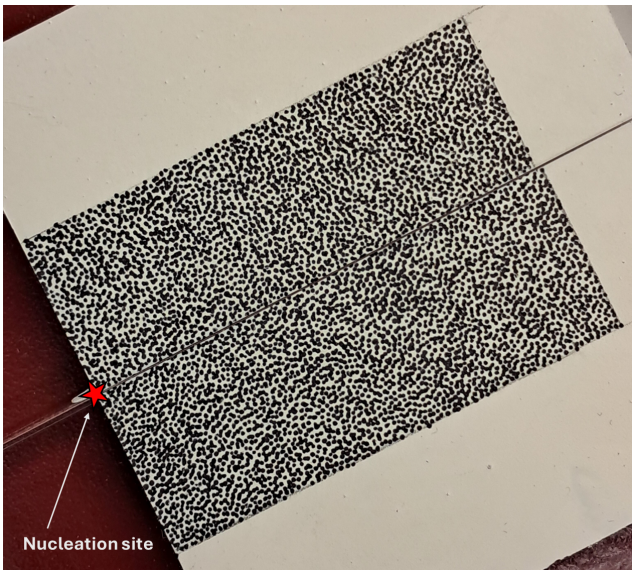


Figure 3.3: Example of speckle pattern.

3.2 Experimental setup

Figure 3.5 shows the experimental setup, which is part of the laboratory equipment at the California Institute of Technology. A similar setup was used to study the dynamic propagation of supershear ruptures and sub-Rayleigh ruptures with the aid of DIC ([3, 16, 17, 18]) while other studies ([19, 20, 9]) relied only on heterodyne laser velocimetry.

To induce at the interface a shear stress state coupled with a normal stress state,

the specimen with the inclined interface is loaded with uniaxial compression using a hydraulic press (Instron 300LX).
The diagnostics include:

- ultrahigh-speed camera (Shimadzu HPV-X): it records 128 images at 5 million fps, so an image is captured after every 0.2 µs. Each image has a shape of 400 x 250 pixels^2;
- high-voltage capacitor bank (Cordin 640): charged to a voltage of 2 kV, it is responsible for a sudden discharge that causes the Ni-Cr wire to be heated and transformed into high-pressure plasma;
- pulse/delay generator (Model 575, BNC), to introduce controlled delay between individual elements of the diagnostics;
- oscilloscope (Tektronix DPO 3034) to monitor and register the various signals, like that from the laser velocimeters and the capacitor discharge. The signal from the capacitor, which triggers the high-speed camera, is used to set time $t = 0$;
- two Polytec heterodyne laser velocimeters, each consisting of a sensor head (Polytec OFV-511 andOFV-551) and a controller (Polytec OFV-5000 VD-02 and VD-09).

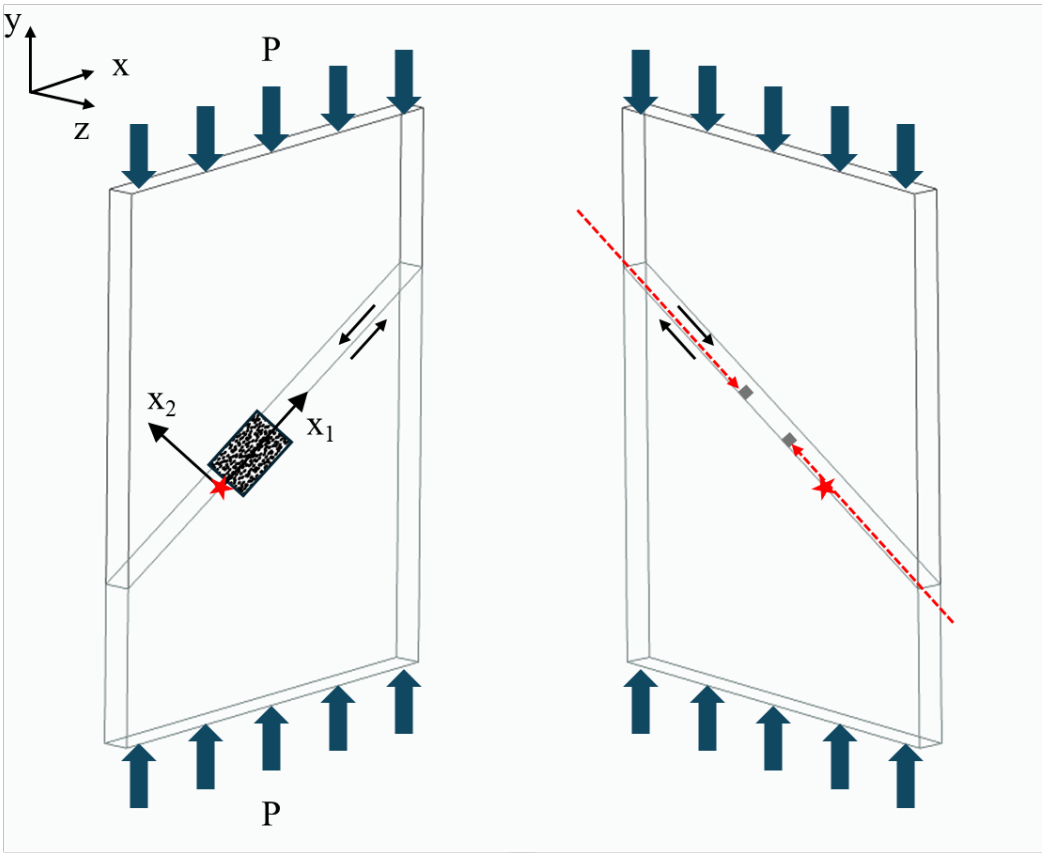


Figure 3.4: Experimental setup scheme.

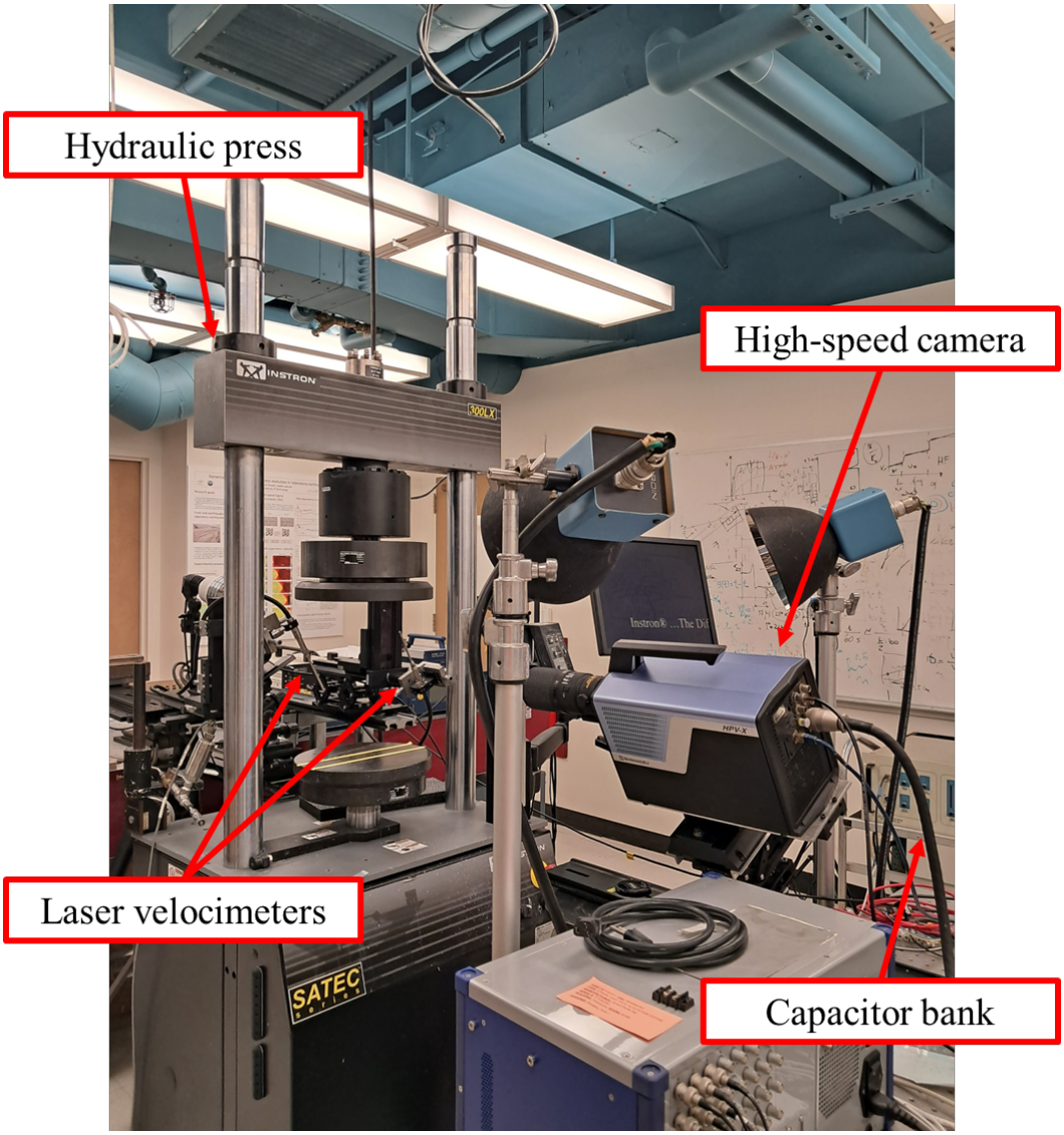


Figure 3.5: Experimental setup.

3.2.1 Heterodyne laser velocimetry

Heterodyne laser velocimetry is a technique which allows to record the component of the particle velocity aligned with the laser beam at discrete locations. The principle behind it is the Doppler effect: a wave reflected by a moving object results in a change of frequency in the reflected wave itself. Specifically, the particle velocity component induces a Doppler frequency shift, causing the resulting frequency signal to be different from the frequency of the reference beam. The signal is positive when the movement is towards the sensor head, instead it is negative if the particle moves away from it.

When data is acquired by the oscilloscope, 1 V corresponds to 1 m/s. Furthermore, the two controllers have different output decoders: the VD-02 output decoder has a bandwidth of 1.5 MHz and a resolution of 0.15 µm/s while the VD-09 output decoder has a bandwidth of 2.5 MHz and a resolution of 0.25 µm/s. Moreover, they can measure particle velocities up to ±10 m/s. In conclusion, they are perfectly suitable to measure particle velocity in this type of experiments [19].

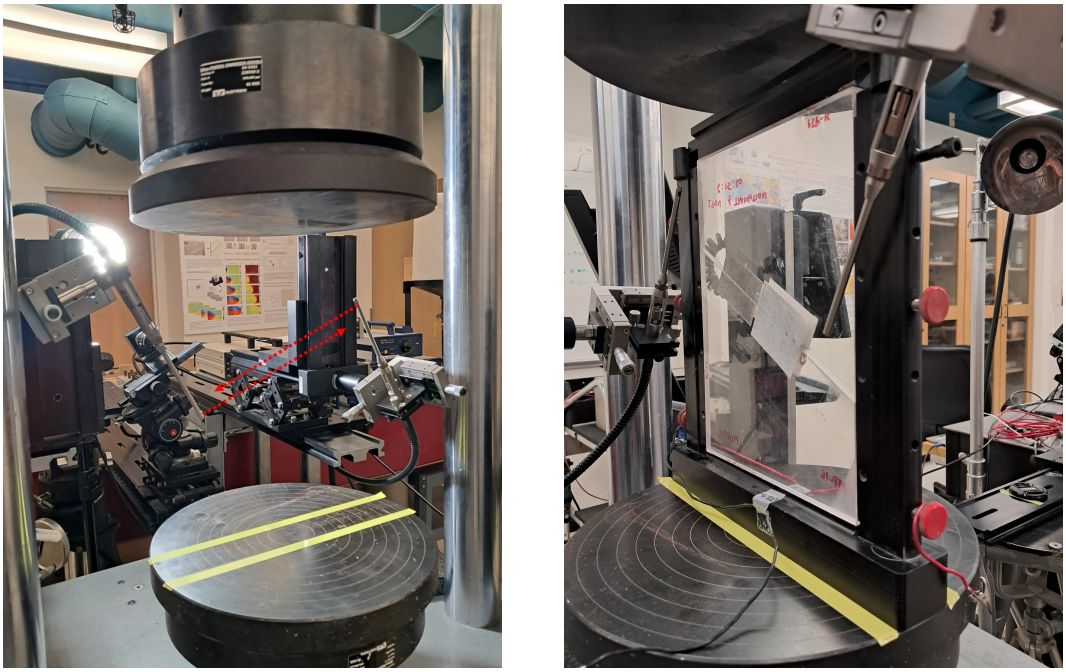
It is noteworthy to mention that the VD-09 decoder has a delay of 4.9 µs with respect to the VD-02 controller [9] due to a different circuit design, a delay that has to be taken into account when processing data acquired with the velocimeters.

3.2.2 Laser velocimeters support system

The support system for the laser velocimeters plays an important role in their use: it must have enough degrees of freedom to allow for a good positioning of the probes and, at the same time, it must be sturdy and stable as much as possible in order to guarantee an easy and good tuning. Generally, one proceeds first by coarse and then by fine tuning of the position of the probe

and consequently of the laser beam.

Two independent support stations were built (Figure 3.6) so as to have independent measures. Additionally, a probe that redirects the laser beam by 90° is employed to get as close as possible to the specimen. This allows to reduce measurement errors introduced by misalignment of the optic axis with the direction of the particle velocity component that needs to be measured.



(a) (b)

Figure 3.6: Laser velocimeters setup.

3.2.3 Reflective tapes

In order to reflect the laser beam at specific points on the specimen, rectangular reflective tapes of approximately 2×2 mm^2 in size are applied on its surface. The two reflective tapes used to measure the particle velocity are positioned on the top plate and on the opposite side of the specimen with respect to the side with the speckle pattern (Figure 3.6b). The idea is to use the two points to obtain a relative measure of the particle velocity. To maximize the precision of the location where the measure is taken, the reflective tapes are positioned

based on the tape corner that is preserved as sharp as possible when cutting the tape with a knife [9]. The laser beams hit the reflective tape as shown in Figure 3.7.

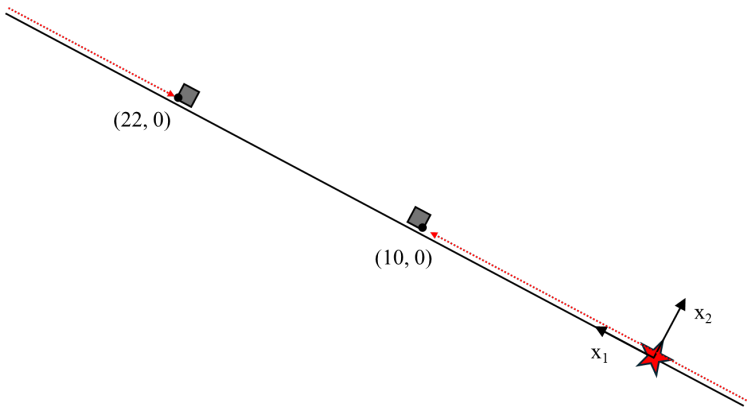


Figure 3.7: Laser beams and reflective tapes scheme. Tape corner coordinates are in millimeters.

3.3 Test procedure

When ready to be tested, the interface surface is cleaned with Isopropyl alcohol so as to remove any bead-blasting residue or any unwanted particles in general.

The Ni-Cr wire is then placed in the designated notch on the lower plate, making sure that it is perfectly embedded in the surface. Two pieces of tape on each side of the specimen ensure that the wire stays in place before placing the upper plate on the lower one.
Afterwards, both the bottom and the top plate are positioned into the specimen holder (Figure 3.8) which ensures that there is no misalignment: the holder keeps the specimen vertical and the two plates aligned. Three screws on each side are lightly tightened before loading in order to avoid sliding during the loading phase, especially at higher interface angles.

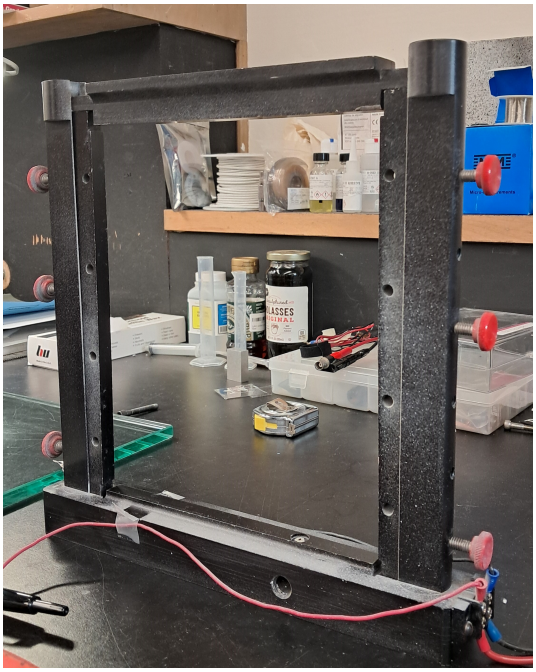


Figure 3.8: Specimen holder.

The specimen holder is placed on the hydraulic press, where its position has been marked with yellow tape (Figure 3.6) before the first experiment to minimize both the adjustments needed to position the laser beams and the differences between each experiment.
With the aid of a measuring tape, the perpendicularity of the specimen surface to the camera is verified. This is particularly important for the 2-dimensional digital image correlation.

The moment in which the two plates come into contact sets the start of the timer that monitors the holding time. It is a quantity that is monitored because it relates to the state of the interface from a frictional point of view, since it causes a change in the state variable θ.

The target load is set on the hydraulic press so as to obtain a resolved interface-normal stress σ_0 of 12.51 MPa for all tests. This means that the far-field load P that simulate the tectonic stress is:

- 16.05 MPa for the tests with $\alpha = 28°$

- 15.00 MPa for the tests with $\alpha = 24°$

These values of P are used in other studies because, together with α, they allow to generate dynamic ruptures.

The equations that relate σ_0 and the corresponding resolved shear stress τ_0 to P are the following:

$$\sigma_0 = P \cos \alpha^2 \tag{3.1}$$

$$\tau_0 = P \cos \alpha \sin \alpha \tag{3.2}$$

Once the hydraulic press is started, the moving crosshead starts to rise at a speed of 0.2 mm/min and when the load reaches 1 kN the screws on the sides of the specimen holder are unscrewed. Consequently, the specimen is now unconstrained. The moving crosshead stops when the target load is reached.

At this point, the laser beam from the laser velocimeters is focused on the reflective tape corner, the high-speed camera is positioned in order to ensure that the interface is aligned with the pixels and positioned at half of the image captured. In this way, the interface does not cross diagonally the pixels.
To check the brightness of the recorded images, a sequence of images are captured with the high-speed camera.
A ruler is then placed on the specimen and another sequence of images is recorded to have a measure of the pixel scale.
A black tape cover is applied as near as possible to the nucleation site to minimize the visibility of the explosion flash on the images recorded by the high-speed camera.

Finally, the alligator clips connected to the high-voltage capacitor are attached to the Ni-Cr wire (Figure 3.9) and the explosion is triggered. Once the test is finished, the instant in time when the first image is recorded, in relation to the trigger, is noted in order to correctly compute the time.



Figure 3.9: Specimen setup right before the wire explosion.

3.4 Digital Image Correlation

Digital image correlation (DIC) combined with ultra-high speed photography is used to measure the full-field displacement resulting from the shear rupture nucleation. Strain and stress components are calculated following the constitutive law for a linear elastic medium after the correlation has identified the displacement fields on the sequence of captured images. The key factor that plays an important role in the use of DIC to investigate shear ruptures is how it allows to have quantitative measures instead of the qualitative observations obtained with the use of photoelasticity.

The field of view (FOV) has a width of 30 mm and a height of 20 mm circa (Figure 3.10): for each experiment the distance from the nucleation site is measured with a caliber, while the exact dimension of the FOV is calculated from the picture of the ruler taken before starting the test, which allows to know the dimension of a pixel. The FOV is positioned on one side of the

nucleation site assuming that there is symmetry with respect to the plane that contains the nucleation site and that is perpendicular to the FOV itself [15]. In fact, in this type of experiments, two ruptures start propagating on each side of the wire notch.

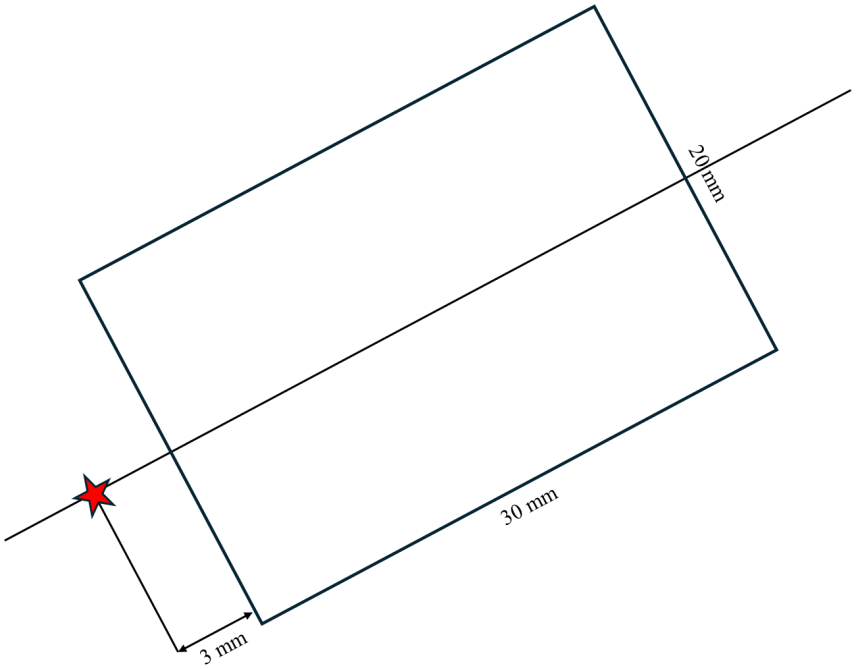


Figure 3.10: Field of view.

The correlation software used to process the images recorded by the high-speed camera is VIC-2D and the correlation is with respect to the first image captured, prior to the rupture and the wire sublimation, since the deformations involved in this experiments are small. The step-size is always 1 while the subset sizes used are 41x41 and 21x21 pixels^2. Most of the results shown are obtained with a subset of 41x41 pixels^2 because it translates into less noisy data [18].

When starting the analysis, two rectangular regions are identified, one for the top plate and one for the bottom plate, to avoid interpolating values at the interface, which is a displacement discontinuity. The use of the "Fill boundary" algorithm allows to extrapolate displacements up to the boundaries.

The flash resulting from the wire sublimation is visible for all tests, thus

affecting the DIC analysis. The flash first appears at 3.34 µs and it lasts 5.88 µs on average. For certain tests it is weaker, hence resulting in cleaner DIC images especially near the interface. In some experiments, debris from the wire explosion is also noticeable (Figure 3.11).

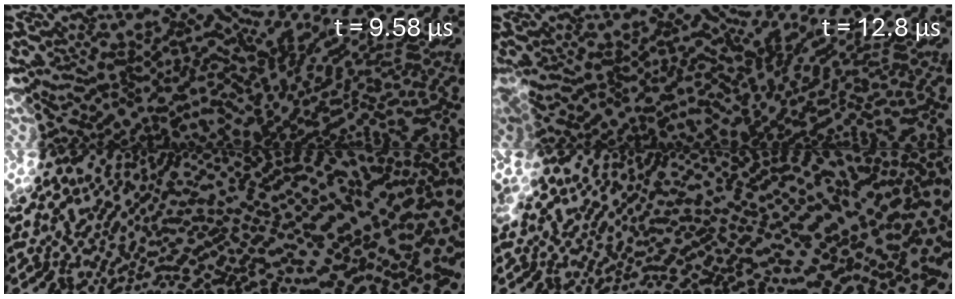


Figure 3.11: Debris from the explosion, especially visible in one of the experiments.

3.5 Data processing

3.5.1 Filtering of oscilloscope data

To filter the output data from the oscilloscope, a 5^{th} order low-pass Butterworth filter is used [9]. It passes signals with a frequency lower than the normalized cut-off frequency ω_c (Equation (3.3)) which is calculated following the Nyquist theorem, which states that, in order to avoid aliasing, a signal must be sampled at twice its highest frequency.

$$\omega_{c,n} = \frac{\omega_c}{\omega_m/2} \tag{3.3}$$

where $\omega_m = 1.25$ GHz is the sampling rate of the oscilloscope while the cut-off frequency ω_c is set to the bandwith of the laser velocimeters.

3.5.2 DIC Post-processing

Data obtained through DIC undergoes a process of up-sampling and filtering. In the up-sampling, the number of points is doubled and the additional points are calculated through linear interpolation. The up-sampled data is then filtered with a Savitzky-Golay filter, which is a digital filter that fits a series of points (window length) with a polynomial of order n. The window length is set to 11 and the polynomial is of order 3.

If interpolation is needed to obtain data at specific locations, the data is first up-sampled and filtered to maintain its "shape" and then linear interpolation is used.

The shown plots are obtained through the Matplotlib library in Python.

3.6 Experiments

The experiments conducted feature two different interface angles in order to investigate if α influences the nucleation process of dynamic ruptures. For each test the holding time is monitored and is reported in Table 3.1.

α	**Test number**	**Holding time**	**FOV**
24°	/	17min	Intermediate
28°	1	1 h 10 min	Intermediate
	2	2 h 8 min	Intermediate
	3	18 min	Intermediate
	4	1 h 14 min	Small

Table 3.1: Experiments conducted.

3.7 Finite element simulation

The FE code used in the simulations is PyLith, specifically the version 2.2.2 and the tetrahedral mesh (Figure 3.14) is generated by means of the LaGrit library (Los Alamos Grid Toolbox). The points in the mesh are connected following three-dimensional Delaunay triangulations to identify each tetrahedral element. The edge length tested are 2 mm and 1.3mm which correspond to 754680 and 2831520 elements respectively. As shown in Figure 3.13, there is not appreciable change. To simulate the frictional interaction at the interface between the two plates, the frictional model used is rate-and-state friction with "aging law":

$$f(V,\theta) = f^* + a \ln \frac{V(t)}{V^*} + b \ln \frac{V^*\theta(t)}{D_{RS}} \tag{3.4}$$

$$\frac{d\theta}{dt} = 1 - \frac{V(t)\theta(t)}{D_{RS}} \tag{3.5}$$

The frictional parameters used in the simulation are the following:

- $f^* = 0.54$;
- $V^* = 1$ µm/s;
- $a = 0.007$;
- $b = 0.030$;
- $D_{RS} = 1$ µm.

It is relevant to highlight that the interface is velocity weakening since $a < b$ and that the parameters are obtained assuming the "aging law" as the state variable evolution law. The value of b should be equivalent to the stronger weakening effect associated with flash heating, even if the phenomenon is not implemented in the friction formulation present in PyLith.

In PyLith, cohesive cells are used to control the relative motion between the

two surfaces in contact at the interface. In particular, cohesive cells are zero-volume cells that allow to have additional degrees of freedom (Figure 3.12) and decouple the dynamics of the two sides of the interface surface. The corresponding discrete system of equations is solved for the increment in slip.

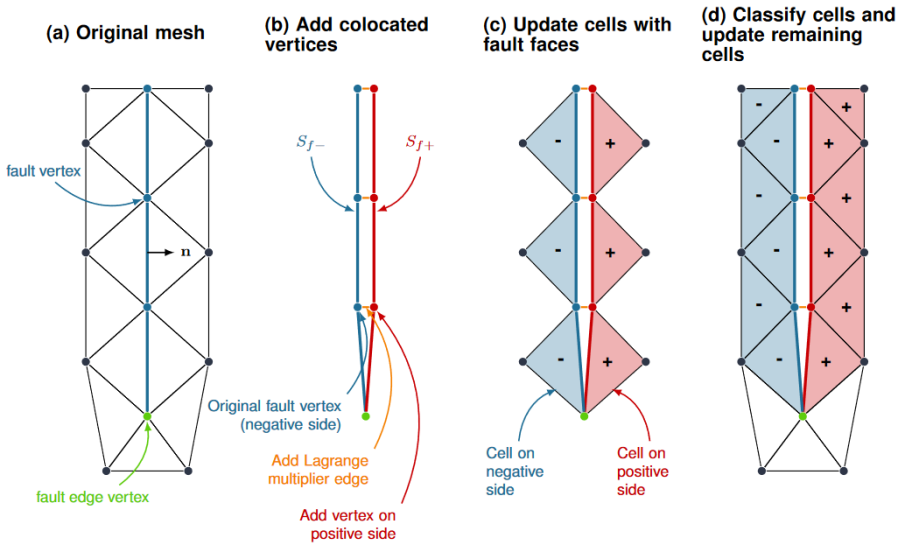


Figure 3.12: Cohesive cells used in the fault implementation [21].

To simulate the uniaxial compression to which the specimen is subjected, a non-zero initial stress state is imposed:

$$\boldsymbol{\sigma}_0 = \begin{bmatrix} 0 & 0 & 0 \\ 0 & -P & 0 \\ 0 & 0 & 0 \end{bmatrix} \tag{3.6}$$

The time stepping formulation is explicit and the time step Δt is uniform:

$$\Delta t = 0.03 \text{ µs} < \Delta t_{stable} = \frac{\text{element length}}{c_p} \tag{3.7}$$

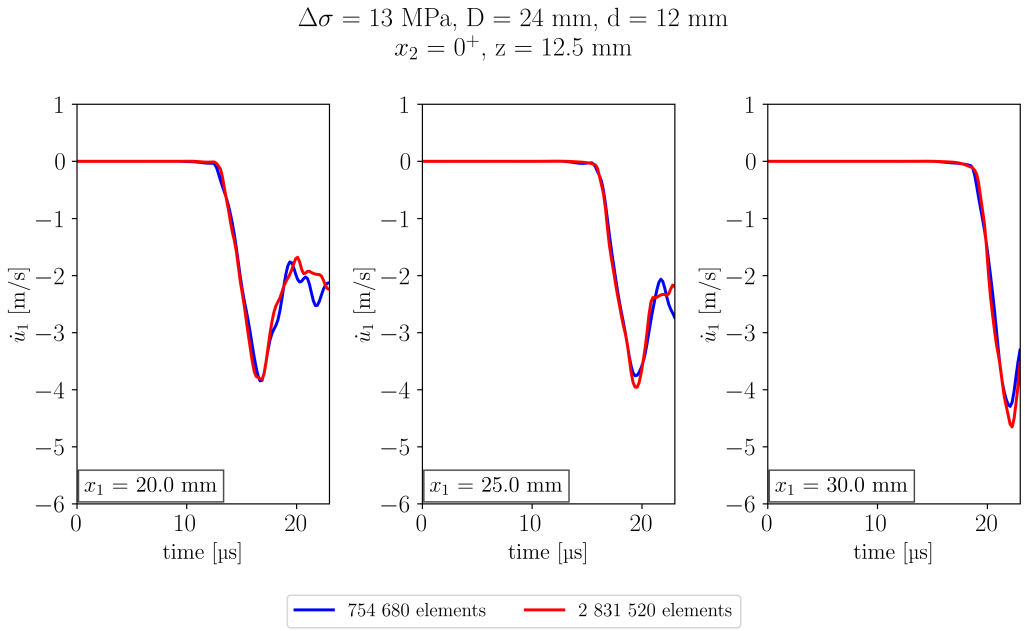


Figure 3.13: Influence of the number of mesh elements on the interface-parallel velocity.

To avoid numerical instability in explicit time-stepping formulations, numerical damping is used: the normalized artificial viscosity is set to the default value of 0.1.

The material model used is istropic linear elastic.

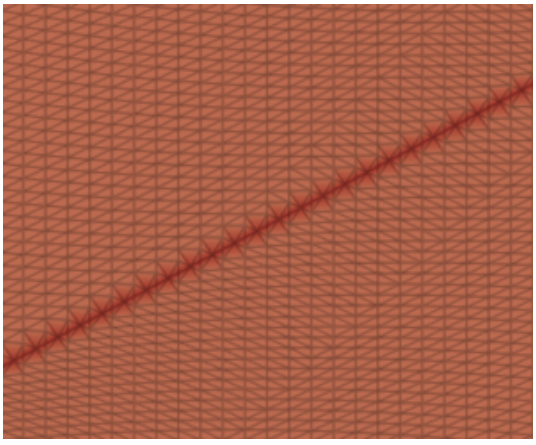


Figure 3.14: Detail of the tetrahedral mesh.

3.7.1 Boundary and initial conditions

To model the contact with the hydraulic press, all degrees of freedom are constrained for both top and bottom surfaces of the specimen.

Concerning the initial conditions, the only variable that is non-zero is the initial state variable θ_0: in this way, we can simulate different holding times. In fact, for any holding time, θ and, therefore, the slip rate V, are both non-zero. Given the holding time, the value of the initial slip rate V_0 is known from the healing curves. From V_0, one can calculate θ_0 to use in the Pylith code:

$$\theta_0 = \frac{D_{RS}}{V^*} \exp\left(\frac{f_0 - f^* - a\ln(\frac{V_0}{V^*})}{b}\right) \tag{3.8}$$

where $f_0 = \tan\alpha$.

3.7.2 Simulation of the nucleation process

To simulate the nucleation process and the decrease in the interface-normal stress σ_{22} caused by the wire explosion, a spatio-temporal variation of σ_{22} is imposed (Figure 3.15) on the interface [22]. To later compare the numerical simulation with the data from the experiments, the instant in time where the interface-normal stress starts changing is set to be equal to 2 µs. It is assumed that there is no difference along the z axis in the spatio-temporal variation of the resolved normal stress.

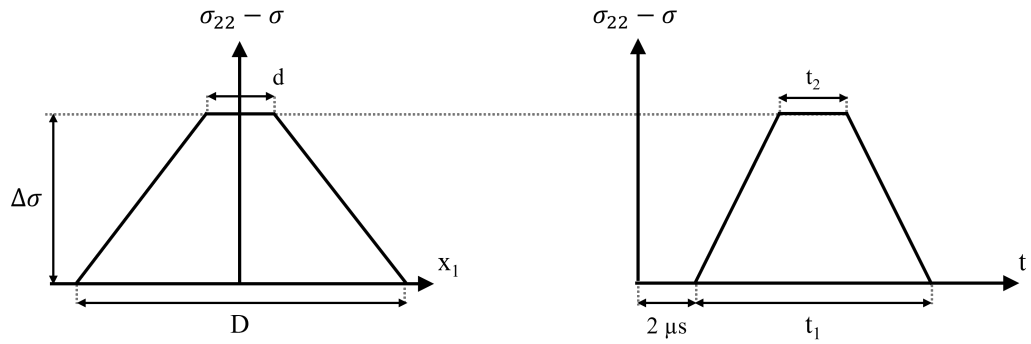


Figure 3.15: Spatio-temporal variation of the interface-normal stress to simulate the Ni-Cr wire sublimation.

Chapter 4

Results and Discussion

The following results focus first on experimental data, starting from the calculation of the P-wave speed, which is then used in the tracing of the P-wave front resulting from the explosion. The stress state is then explored to understand how it is perturbed by the Ni-Cr wire sublimation and a possible dependence of the nucleation features on friction and interface angle is considered. Ultimately, the importance of friction on the study of shear ruptures is emphasized. Subsequently, results from the finite element simulation are analyzed in order to understand which parameters best simulate the experiments and to examine those quantities that cannot be observed with a two-dimensional analysis.

For the local coordinate system $\mathbf{x} = (x_1, x_2, z)$ shown in Figure 3.4, we can the define the displacement vector (4.1) and the velocity vector (4.2):

$$\boldsymbol{\xi}(\mathbf{x}, t) = (u_1(\mathbf{x}, t), u_2(\mathbf{x}, t), w(\mathbf{x}, t)) \tag{4.1}$$

$$\dot{\boldsymbol{\xi}} = (\dot{u}_1, \dot{u}_2, \dot{w}) \tag{4.2}$$

In terms of interface variables instead, it is possible to define the slip (4.3), the

slip rate (4.4), the out-of-plane slip (4.5) and the corresponding slip rate (4.6):

$$\delta = u_1^{0^-} - u_1^{0^+} \tag{4.3}$$

$$V = \dot{u}_1^{0^-} - \dot{u}_1^{0^+} \tag{4.4}$$

$$\delta_z = w^{0^-} - w^{0^+} \tag{4.5}$$

$$V_z = \dot{w}^{0^-} - \dot{w}^{0^+} \tag{4.6}$$

The superscripts 0^+ and 0^- refer to points on the interface belonging to the top and lower plate respectively.

It is important to note that the interface-normal stress is reported using the geophysical convention, according to which a compressive stress state is positive and a tensile stress state is negative.

4.1 P-wave speed

The interface-parallel velocity ui_1 obtained from the laser velocimeters is used to calculate the P-wave speed: considering the arrival of the first P-wave to be the first positive peak in ui_1 ($ui_1 \geq 0.3$ m/s), the P-wave speed can be calculated using the relative measure obtained from the two refelctive tapes: c_p amounts to 2.83 ± 0.34 km/s.

To calculate the waves arrival time, a nucleation delay t_{dyn} has to be considered. It represents the delay between the trigger (t = 0) and the first emitted P-wave. In previous works [9, 19] it is reported to be between 4 µs and 6 µs. Given the fact the flash is first visible on average at 3.34 ± 0.19 µs, the nucleation delay is set to 4 μs and the consequent arrival time is shown in Figure 4.1.

Moreover, observing the interface-parallel velocity recorded by the laser ve-

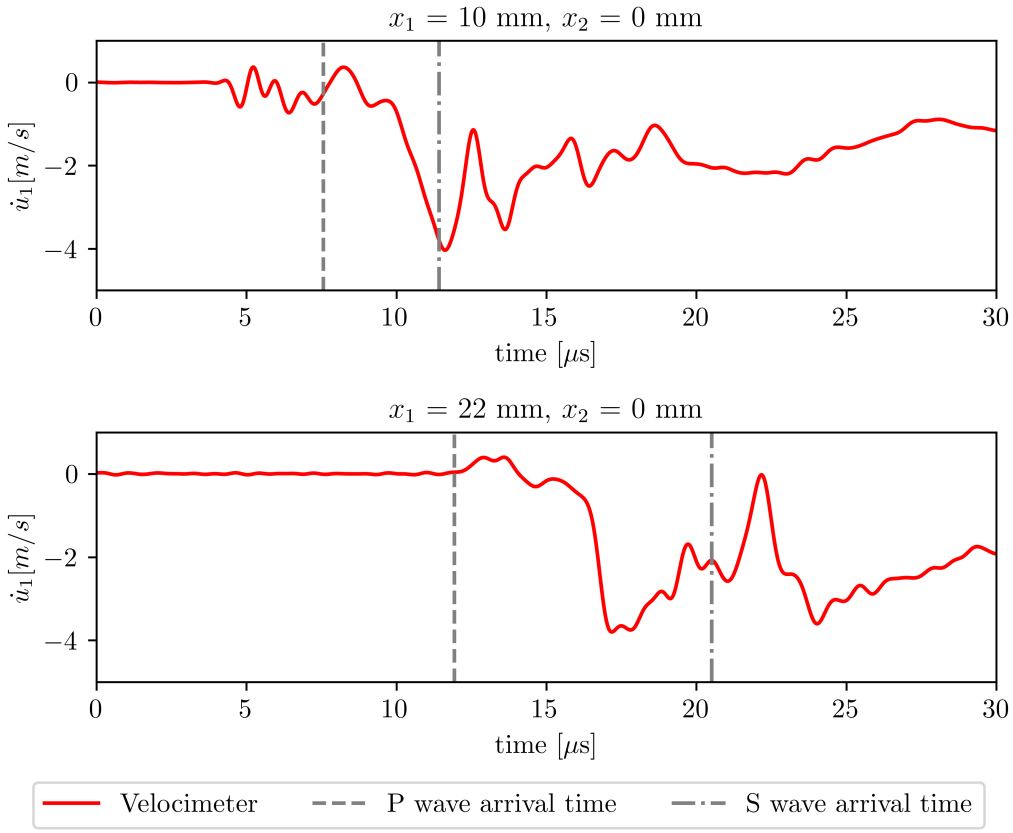


Figure 4.1: Interface-parallel velocity obtained from the laser velocimeters with P-wave and S-wave arrival times for $\alpha = 28°$ (test 1).

locimeters allows to determine whether the rupture is supershear or not: in Figure 4.1 we can recognize the drop in $\dot{u}_1$ associated with the rupture arrival and if we look at the point that is located 22 mm from the nucleation site, it is clear how the rupture arrives before the S-wave, which means that it travels at a speed higher than c_s.

It is important to note that the velocity fluctuations that appear at 10 mm from the nucleation site are not physical in nature: instead, they are caused by interference with the nucleation process. In fact, in the experimental setup, the wire notch is positioned between the reflective tape and the laser probe (Figure 3.6). Two independent measures obtained with both the laser velocimeters pointing at 10 mm show the absence of these initial oscillations (Figure 4.2). In this case, the wire notch is not in-between any reflective tape

and the corresponding laser beam.

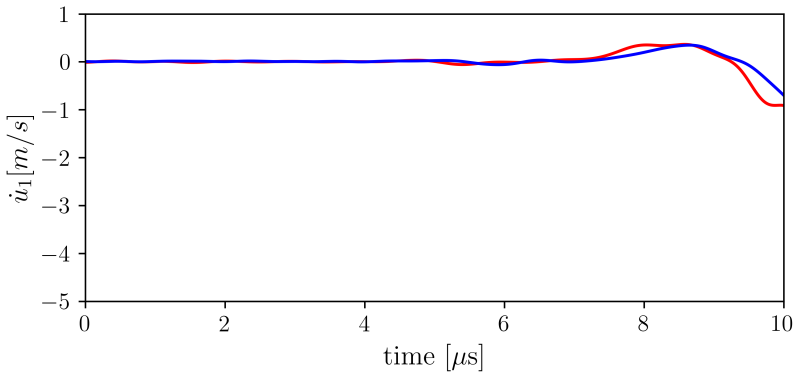


Figure 4.2: Two independent measures obtained with the laser velocimeters positioned at 10 mm from the nucleation site for a specimen with $\alpha = 28°$.

If we compare the particle velocity records obtained with the velocimeters to those obtained through digital image correlation (Figure 4.3), we can see that, in terms of velocity, DIC fails to capture the first positive peak in interface-parallel velocity associated with the P-wave arrival, since its order of magnitude is the same as the order of magnitude of the noise fluctuations.

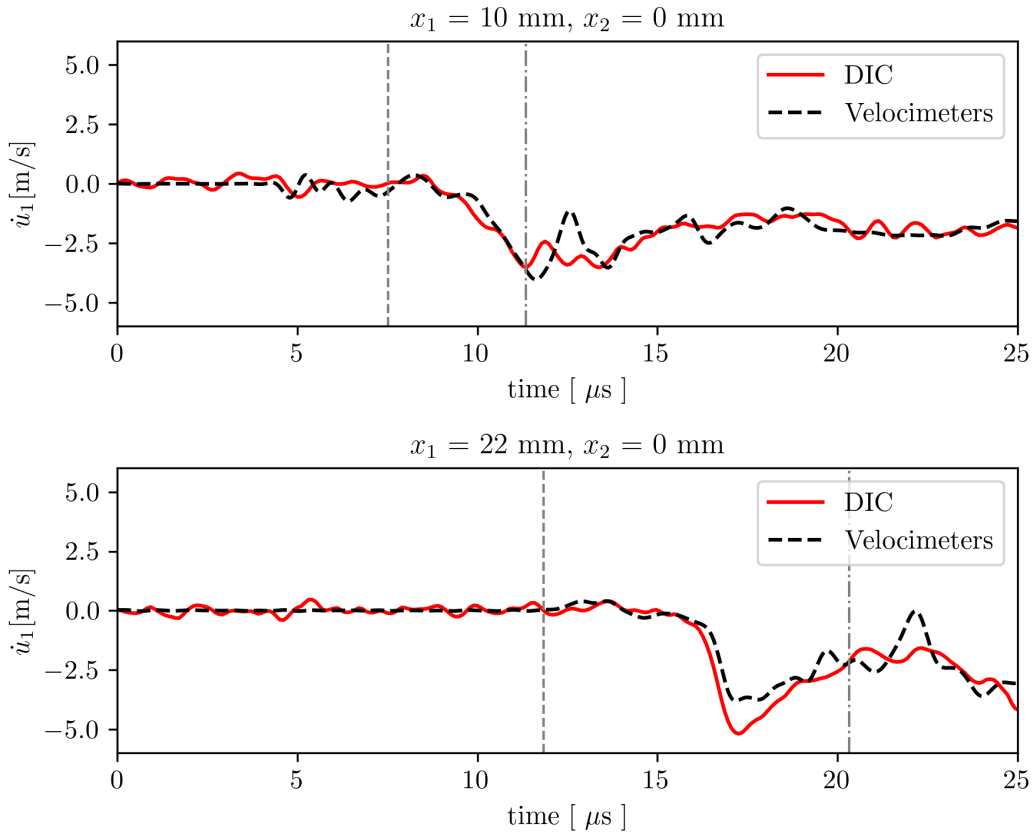


Figure 4.3: Comparison of the interface-parallel velocity obtained through DIC and laser velocimeters for $\alpha = 28°$.

4.2 P-wave front

To observe the P-wave front, the volumetric strain rate $\mathrm{tr}(\dot{\boldsymbol{\varepsilon}})$ is investigated. As a matter of fact, the trace of the strain rate tensor represents the rate of variation of the volume, hence it is a quantity particularly sensitive to detect displacements resulting from dilation and compression. For this reason, it has been successfully used to experimentally measure pressure shock fronts in ultra-fast shear ruptures occurring in viscoelastic materials [15]. Numerically, $(\dot{\boldsymbol{\varepsilon}} = \Delta\boldsymbol{\varepsilon}/\Delta t)$, where Δt is the time difference between two frames.

Using the previously calculated c_p, the theoretical wave speed front (red line in Figure 4.4) is determined assuming a cylindrical wave front centered in the

wire notch ($x_1 = 0, x_2 = 0$):

$$r = c_p \left(t - t_{dyn}\right) \tag{4.7}$$

$$x_1 = r \cos \beta \tag{4.8}$$

$$x_2 = r \sin \beta \tag{4.9}$$

where β is the angle formed with the x_1 axis.

The wave front emitted from the explosion is compressional and stronger in the lower plate, where the wire notch is located. This suggests that the intensity of the P-wave is asymmetrical. Moreover, The explosion wave front is visible after the effects of the flash are negligible at 8 µs and then it starts to fade after $11 - 12$ µs, which might be an effect caused by viscoelasticity. There are no noticeable differences between the test with $\alpha = 24°$ and the one with $\alpha = 28°$.

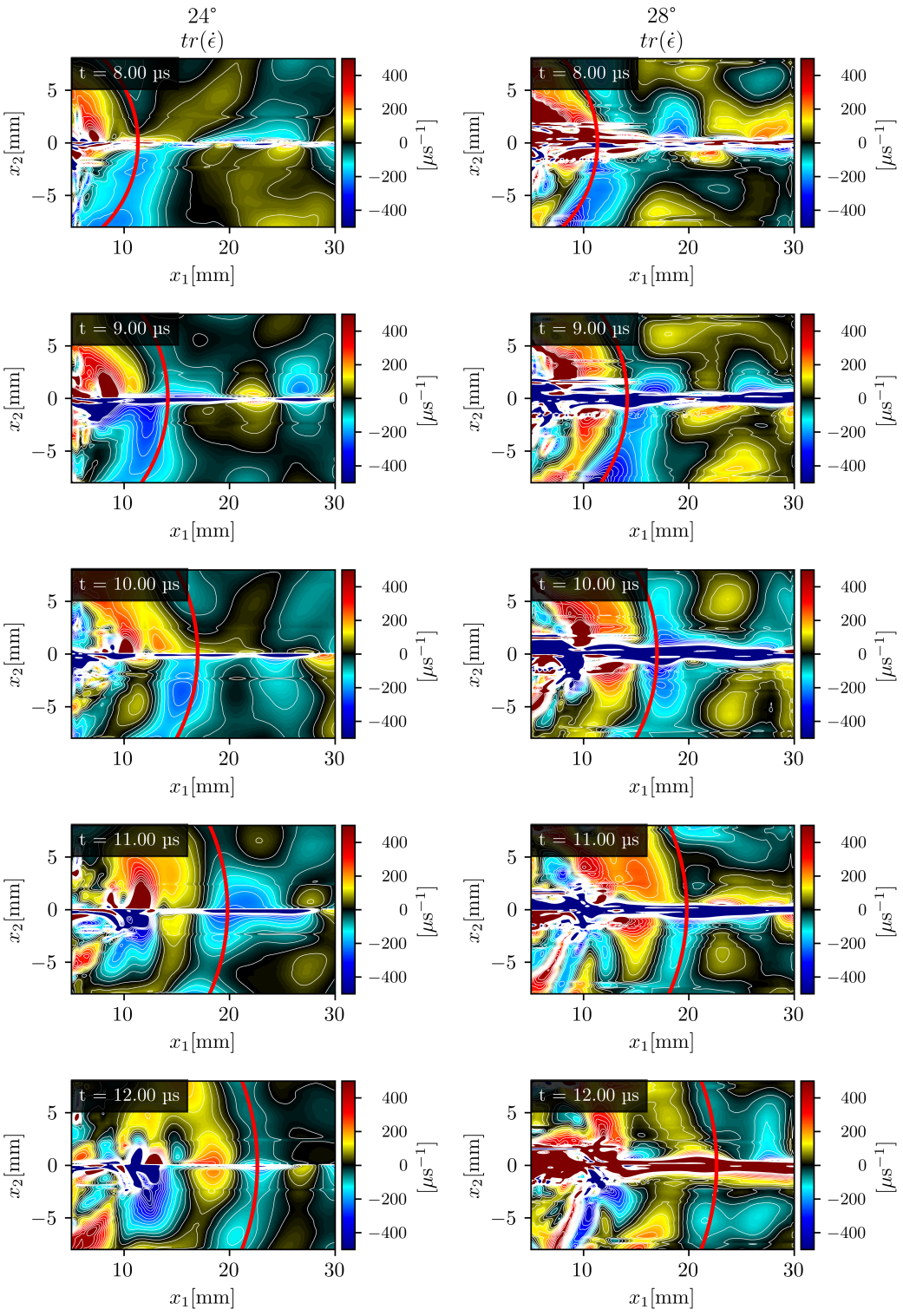


Figure 4.4: Volumetric strain rate field showing the propagation of the P-wave front for $\alpha = 24°$ (a) and $\alpha = 28°$ (b).

4.3 Stress state

To investigate how the sublimation of the Ni-Cr wire affects the stress state at the interface, the way the stress changes in time is considered for points close to the nucleation site and to the interface itself.
It is worth mentioning that the gray area in the following graphs refers to those frames where, on average, the explosion flash is visible, hence altering the results.

Regarding the interface normal stress σ_{22}, Figure 4.5 shows how before and after the nucleation σ_{22} equals the stress that derives from the uniaxial compression. With the P-wave arrival, σ_{22} decreases: the compressive state is progressively weaker.

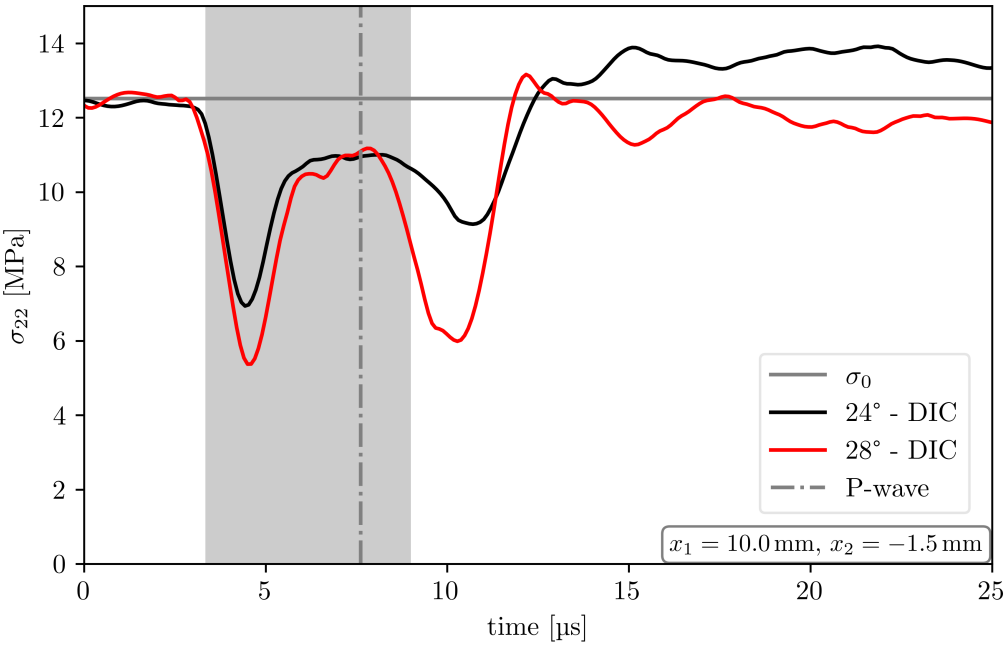


Figure 4.5: Interface-normal stress as a function of time, for a point on the lower plate.

The duration of the interface-normal stress perturbation T is calculated as shown in Equation 4.10 for a point that is 10 mm away from the nucleation

site and on the lower plate. Points closer to the nucleation site ($x_1 < 10$ mm) are affected by the explosion flash.

$$T = t_{90\%} - t_{P-wave} \tag{4.10}$$

where $t_{90\%}$ is the instant in time (after 10 µs) corresponding to $\sigma_{22} = 0.9 \cdot \sigma_0$ and t_{P-wave} is the arrival of the P-wave. The mean value obtained from all the experiments is $T = 4.55 \pm 0.82$ µs.

To identify the region affected by the decrease in the interface-normal stress, the test at 24° is considered, since it is the one where the explosion flash is no more visible after only 6.35 µs. For all the other tests, it disappears after at least 9 µs. The interface-normal stress is plotted as a function of the distance from the nucleation site at 9 µs when the σ_{22} is at its lowest. The point along the interface on the upper plate where the interface-normal stress is 90% of σ_0 is at 12.18 mm from the nucleation site. Consequently, the region affected by the interface-normal stress perturbation has a width of 24 mm assuming symmetry with respect to the nucleation site. If we calculate the point where the interface-normal stress reaches zero, for the lower plate the resulting value is 8.92 mm while for the upper plate it is 4.21 mm. The corresponding average value is 6.56 mm. Consequently, the region where there is opening of the interface is about 12 mm. The decrease in σ_{22} is significantly stronger in the lower plate, where the wire notch is located (Figure 4.6).

How much σ it decreases is difficult to determine since there is asymmetry between the lower and the top plate but it is clear that there is opening of the interface.

If we consider the shear stress instead (Figure 4.7), what is interesting is that, even if starting from different τ_0, the drop in shear stress that is caused by the rupture arrival (Figure 4.8) is up to the same amount.

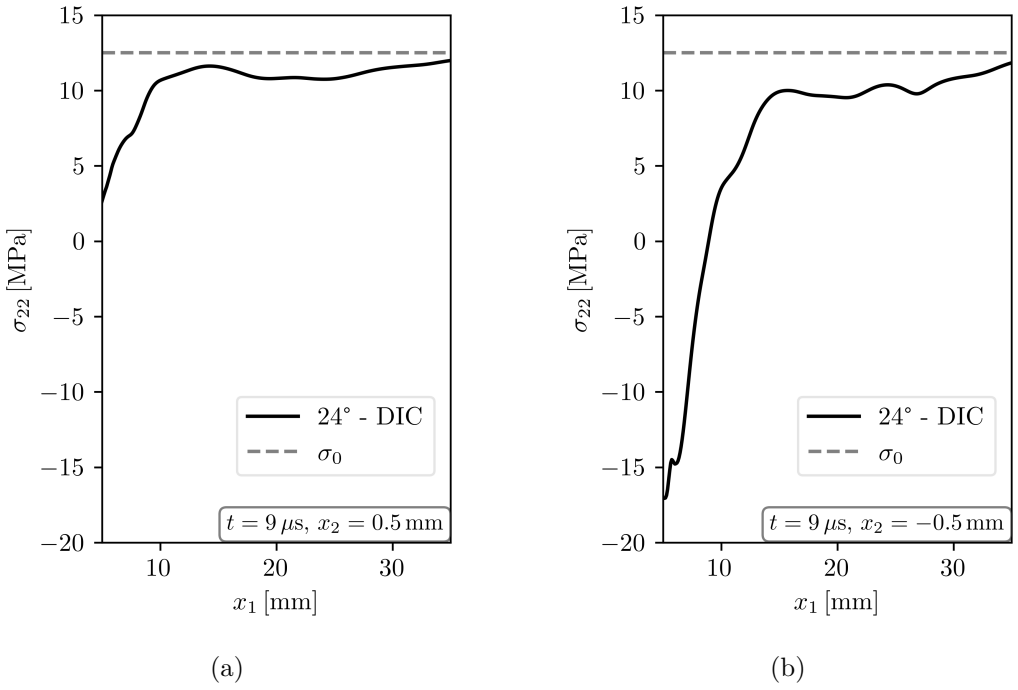


Figure 4.6: Interface-normal stress along the interface on the upper (a) and lower (b) plate at $t = 9$ µs for an angle $\alpha = 24°$.

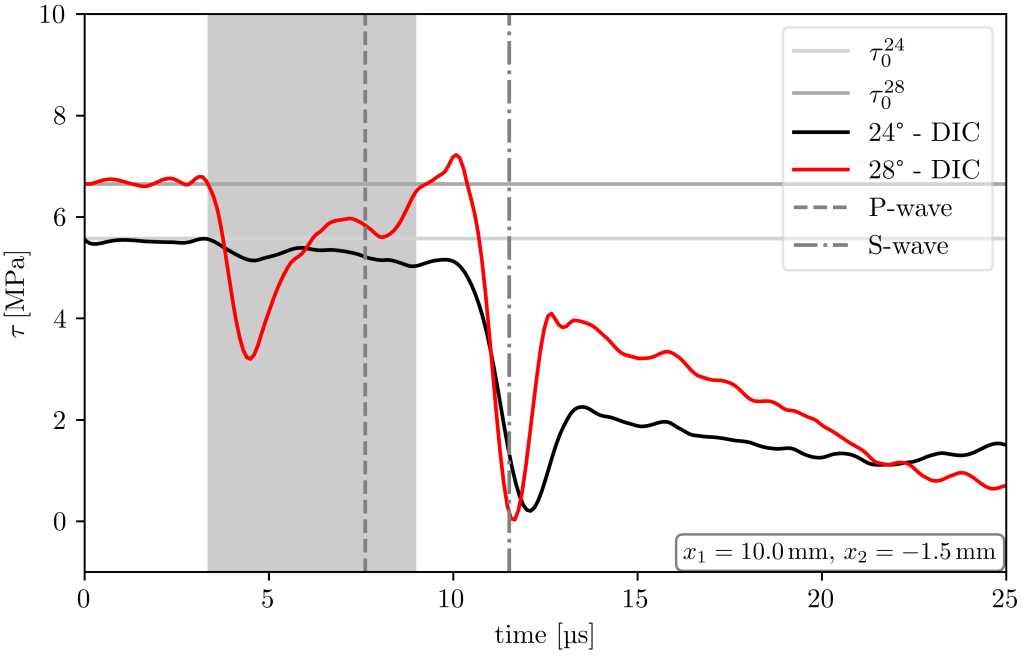


Figure 4.7: Shear stress as a function of time, for a point on the lower plate.

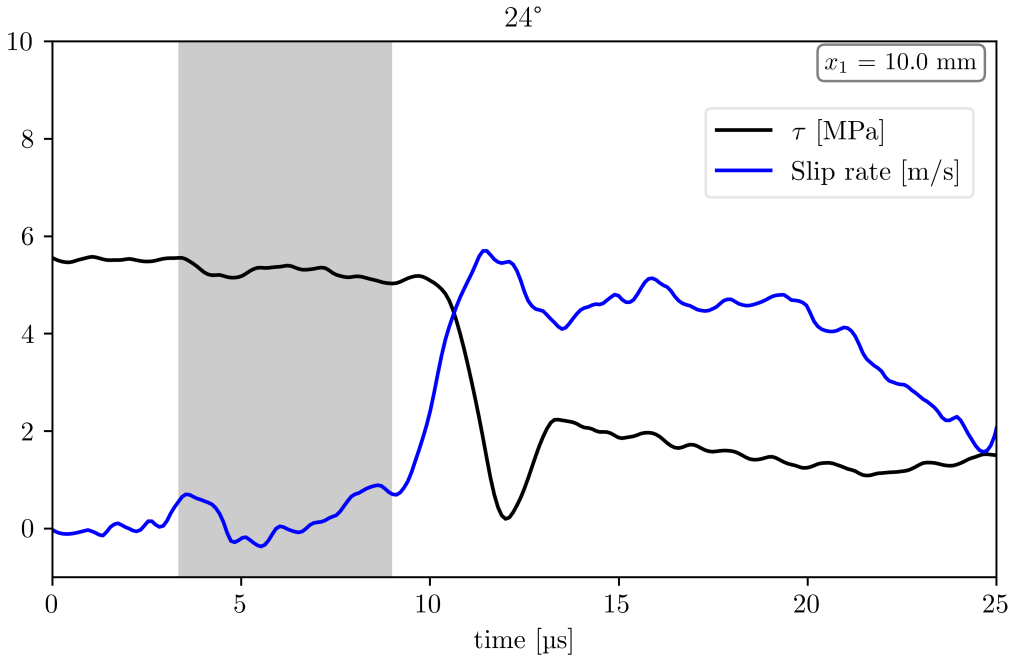


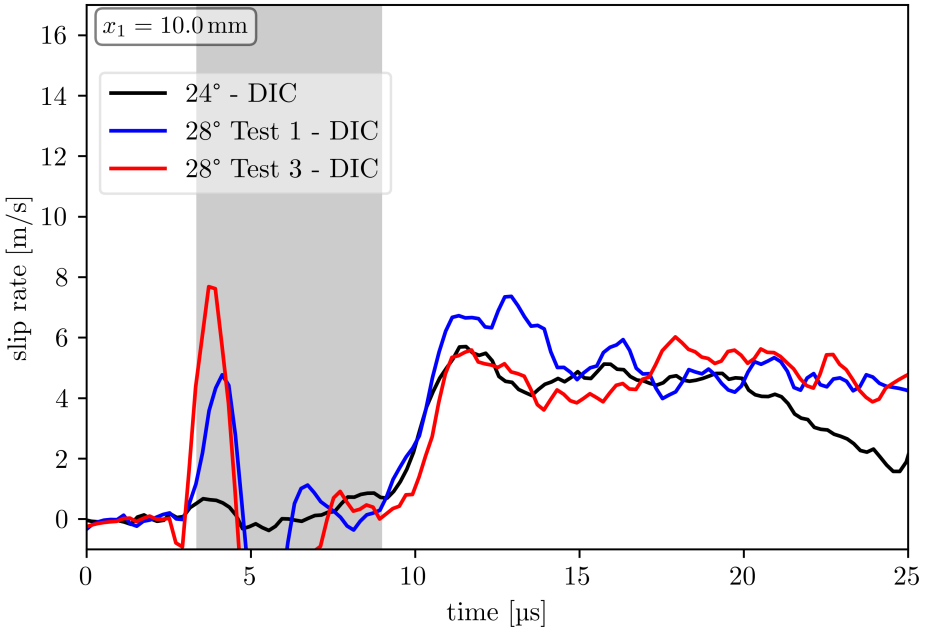
Figure 4.8: Shear stress and slip rate as a function of time for the specimen with $\alpha = 24°$, obtained through DIC.

4.4 Independence of nucleation properties from friction and interface angle

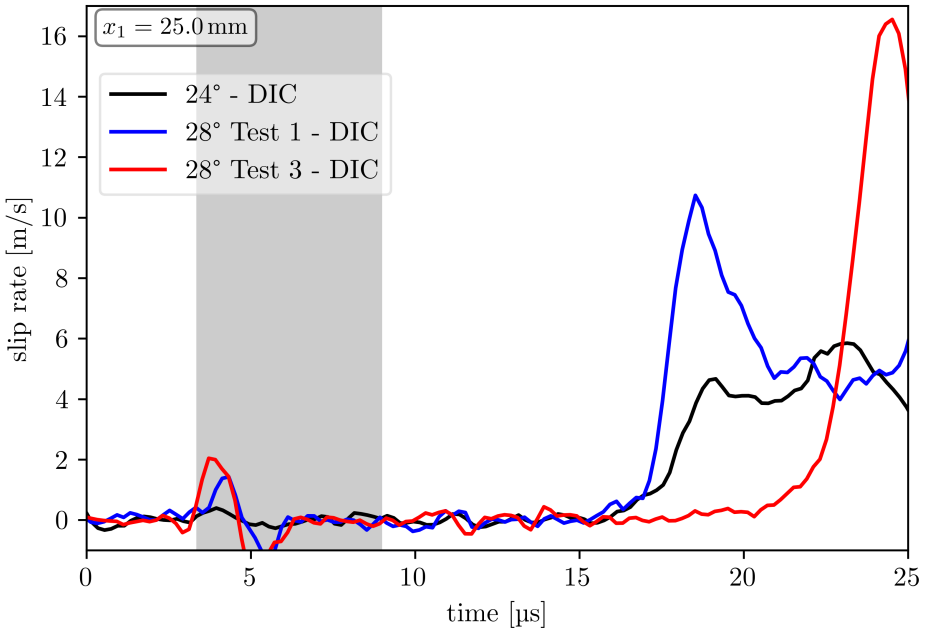
Rupture properties, like rupture velocity and slip rate peak, are heavily intertwined with the frictional characteristics of the interface.
Figure 4.9 shows slip rate as a function of time for different experiments, allowing to investigate the effect of friction and interface angle on the nucleation process. In fact, test 1 and test 3 are conducted with the same interface angle $\alpha = 28°$ but different holding times, while the test with $\alpha = 24°$ and test 3 with $\alpha = 28°$ have different interface angles but the same holding time.

For a point closer to the nucleation site (Figure 4.9a), slip rate properties do not change either with variations in α or with changes in holding time. Instead, if we consider a point further away from the nucleation site (Figure 4.9b), the slip rate presents significant differences, in terms of timing and intensity.
Since the rupture is more developed as it progresses further away from the nucleation site, it is clear that the experiments shown in Figure 4.9 are different from a frictional point of view. Nevertheless, the fact that, closer to the nucleation site, the slip rate at the interface is the same indicates that the nucleation process is independent of friction.

In terms of dependency on the interface angle α, it is evident from Figure 4.9a how there is no difference between experiments conducted on specimens with two distinct α.



(a)



(b)

Figure 4.9: Slip rate at $x_1 = 10$ mm (a) and $x_1 = 25$ mm (b) for tests with different interface angle and holding time.

4.5 Supershear and sub-Rayleigh rupture: the importance of friction

As emerges from the previous paragraphs, friction has a key role in determining the way the rupture propagates, especially its velocity and the magnitude of the corresponding velocity field. In Figure 4.10, two tests are reported: both are experiments conducted on the same specimen but the ruptures are very different. Figure 4.10a shows a supershear rupture, with the Mach cone visible in the interface-parallel velocity and in the shear strain; the interface-normal velocity field is much fainter than the interface-parallel velocity field, as it is typical for supershear ruptures. In Figure 4.10b, the rupture is instead clearly sub-Rayleigh and the interface-normal velocity field is consequently stronger. A symmetry adjustment is used when calculating the variables shown in these colormaps.

Figure 4.11 shows how the slip rate varies in time along the interface. For each point on the interface, there is an instant in time where the slip rate ceases to be zero, which is when the rupture reaches that specific distance from the nucleation site. The inverse of the slope of the line formed by these points represents the rupture velocity. If there is a transition to supershear regime, as in Figure 4.11a, a change in slope is visible when the transition occurs. On the contrary, if there is no transition and the rupture stays sub-Rayleigh while passing through the field of view, the slope remains constant (Figure 4.11b).

It is worth mentioning that the rupture velocity in Test 1 before the transition is the same as the rupture velocity for the sub-Rayleigh rupture in Test 4. Even if the explosion is triggered in the same moment, as can be seen in both Figure 4.11a and Figure 4.11b around 5 µs, Test 4 shows a delay in the rupture arrival.

In summary, it is clear how, in the first place, there is a need to quantitatively

measure the interface surface roughness, in order to avoid discrepancies in the frictional properties of the surface; in fact, the surface preparation process is subjected to human error and leads to slightly different frictional characteristics of the surface when a strict protocol is not followed. A small difference in roughness leads to profoundly different ruptures. Furthermore, the differences between the two ruptures can also be attributed to the corresponding different holding times, which lead to a different state of the interface and thus different frictional features of the interface at the moment in which the rupture is triggered.

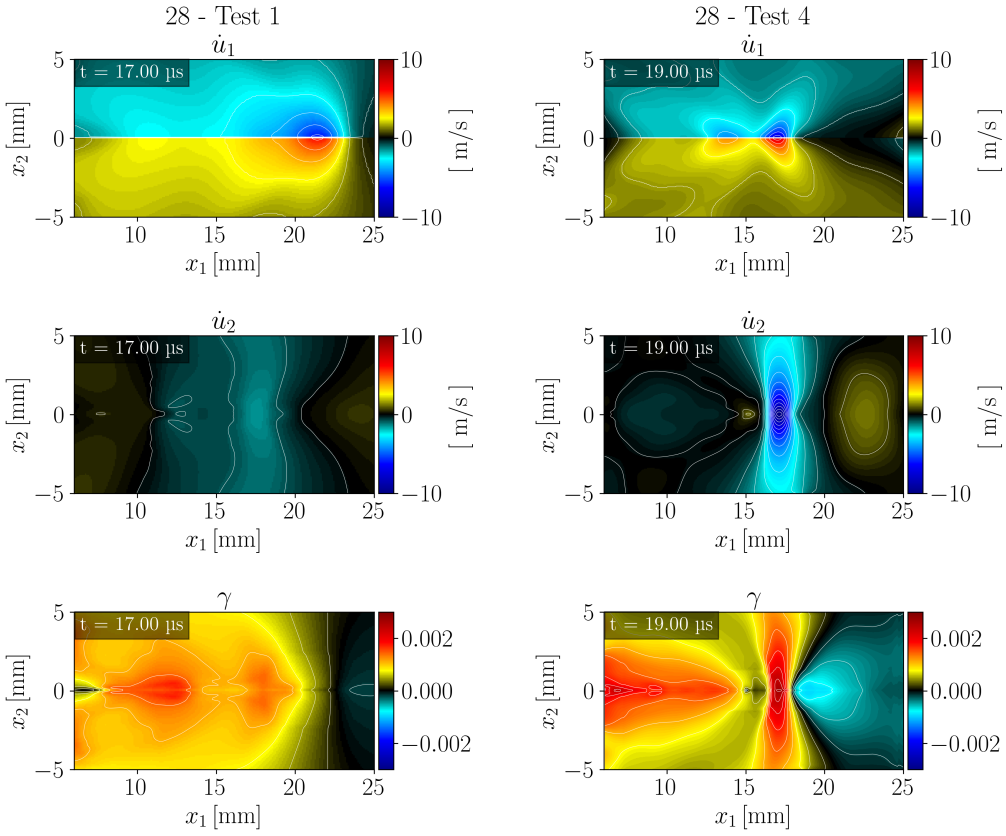


Figure 4.10: Colormaps showing full-field measures of interface-parallel velocity, interface-normal velocity and shear strain for two experiments conducted on the same specimen with $\alpha = 28°$.

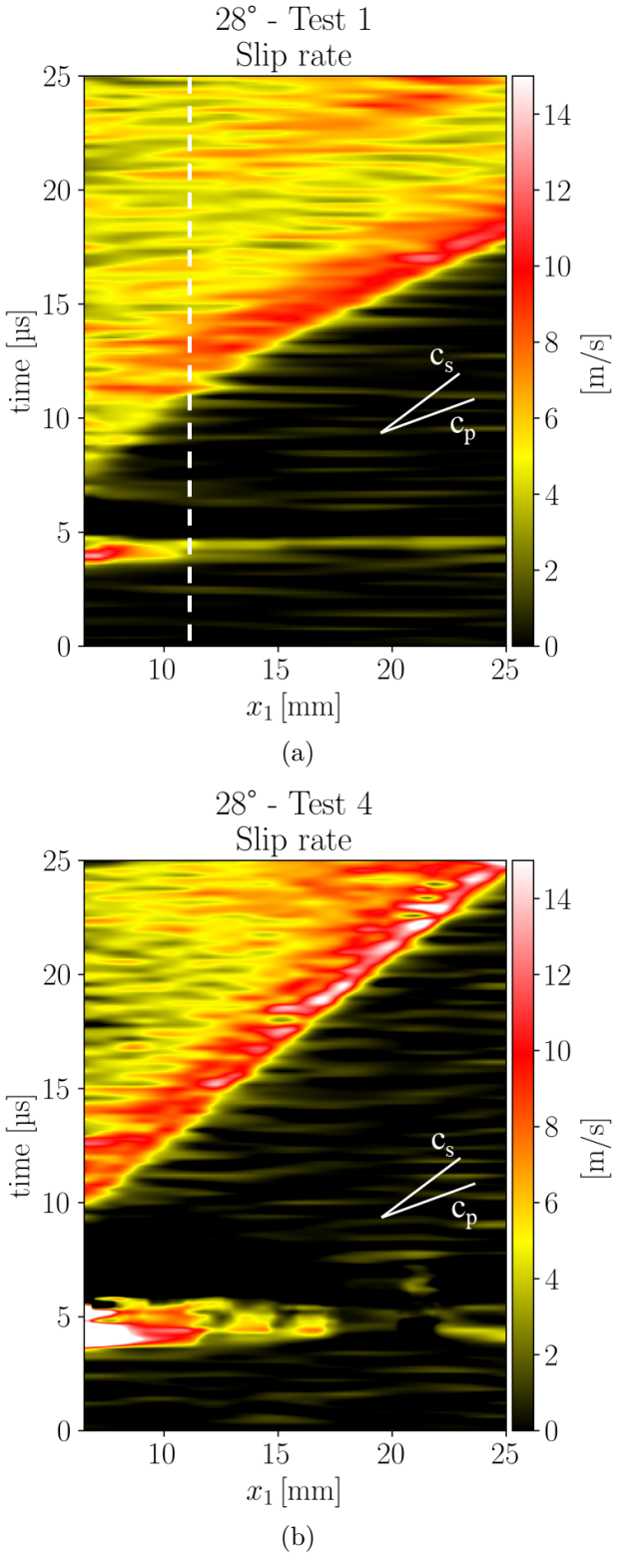


Figure 4.11: Slip rate as a function of time and space.

4.6 FE simulation

The main focus of this study is to investigate the effect of the nucleation parameters on the simulation using data obtained from the experiments, since in previous works [22] they were adjusted to match the arrival of the rupture at a point far from the nucleation site.

The simulated experiment has an interface angle $\alpha = 28°$ and an holding time of 1 h 10 min ($V_{in} = 3.6 \cdot 10^{-10}$ m/s), so that it can be compared to test 1. Specifically, test 1 is chosen because it shows a transition from sub-Rayleigh to supershear regime, which represent an increased complexity in terms of numerical simulation.

In accordance with experimental data, the nucleation parameters used in the numerical simulations are reported in Table 4.1.

Nucleation parameters	
α	28°
t_1	5 µs
t_2	1 µs
D	24 mm
d	12 mm
total simulation time	25 µs

Table 4.1: Simulated nucleation parameters.

It is worth mentioning that, as shown in Figure 3.4, $z = 12.5$ mm represents the "front" surface of the specimen, while $z = 0$ mm is the "back" surface of the specimen.

4.6.1 Influence of nucleation parameters

In general, increasing $\Delta\sigma$ causes the rupture to be faster and to have higher velocity peaks (Figure 4.12). For lower leves of $\Delta\sigma$, no rupture is nucleated.

When imposing a change in the interface-normal stress, if $\Delta\sigma$ exceeds σ_0, the normal stress automatically goes to zero and cannot reach tensile values. This means that for $\Delta\sigma > \sigma_o$ the difference in the result is minimal and it is only due to the fact that the interface-normal stress perturbation is stronger only in the points where $\sigma_{22} - \sigma_0$ never reaches $\Delta\sigma$.

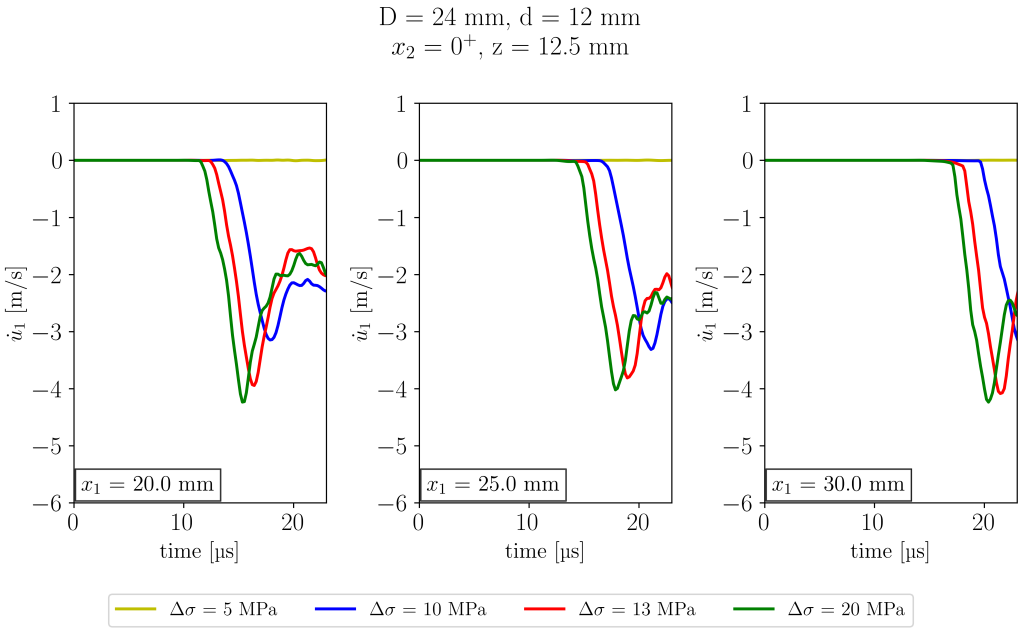


Figure 4.12: Effect of $\Delta\sigma$ on the interface-parallel velocity.

4.6.2 Out-of-plane slip and velocity

The FE simulation reveals that there is slip also in the out-of-plane direction. As shown in Figure 4.13 the out-of-plane slip is equal but opposite on the front and back surface of the specimen. Additionally, $\delta_z(\mathbf{x}, t)$ is antisymmetrical with respect to the plane perpendicular to the specimen surface that contains the nucleation site (Figure 4.14), which suggests that it is caused by the shear

waves associated with the rupture rather than by the Poisson effect. Indeed, if the underlying cause were purely the Poisson effect, there would be symmetry with respect to the nucleation site.

Moreover, if we look at the $\dot{w}_z$ velocity field (Figure 4.14), we can see that it is much weaker than the interface-parallel velocity field. Still, the velocity goes up to ± 2 m/s.

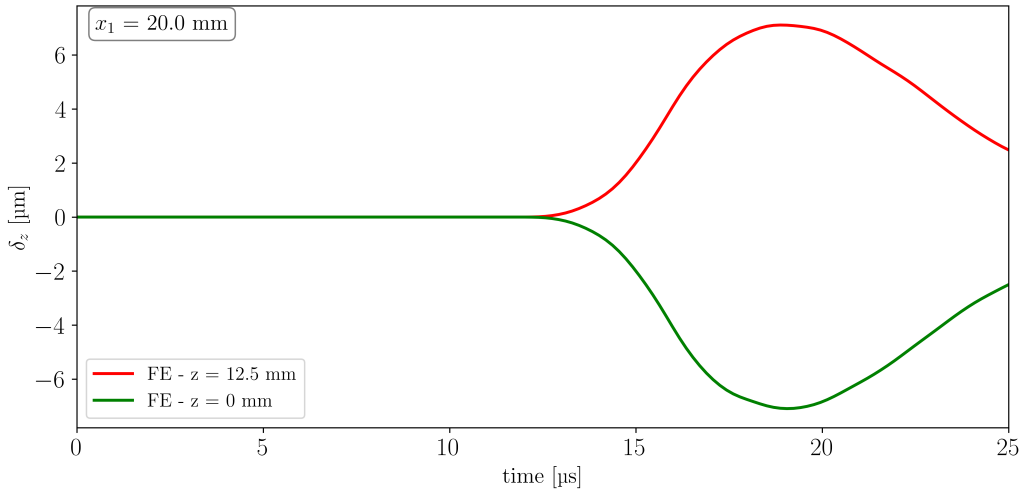


Figure 4.13: Out-of-plane slip for two points located at the same distance from the nucleation site but on opposite sides of the specimen.

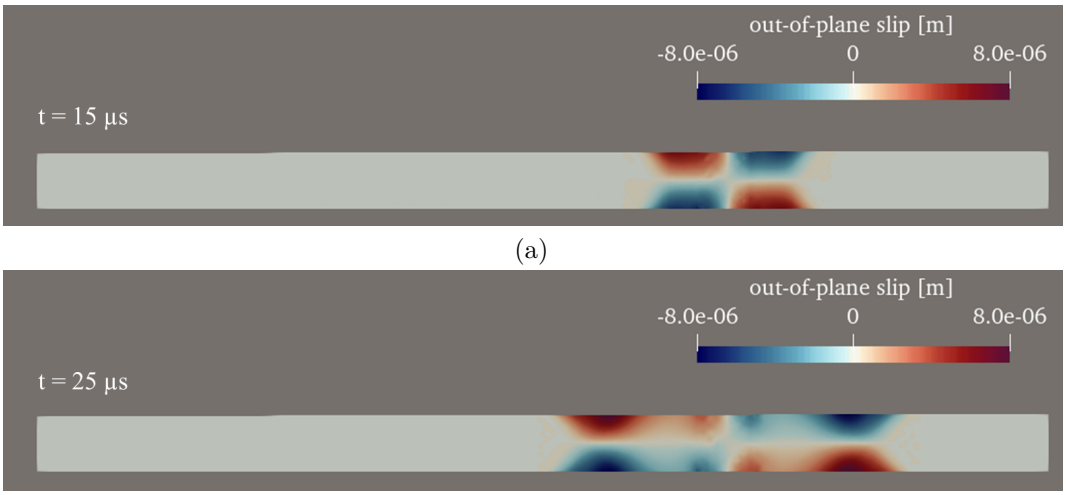
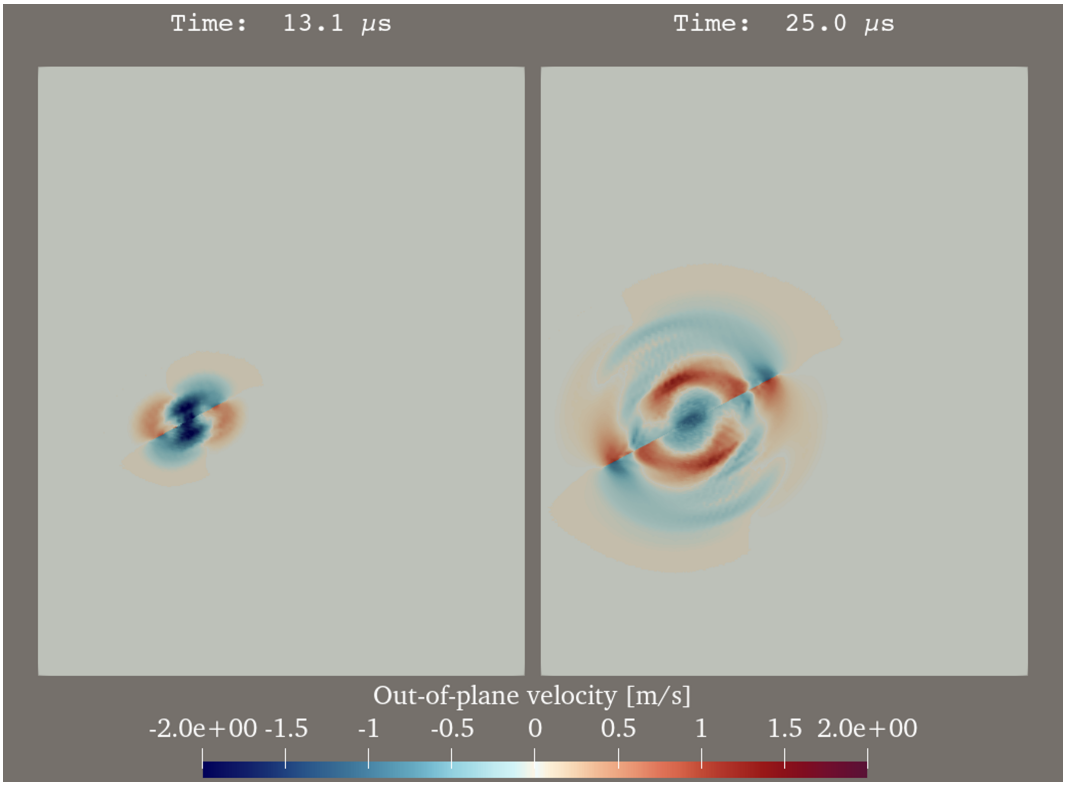
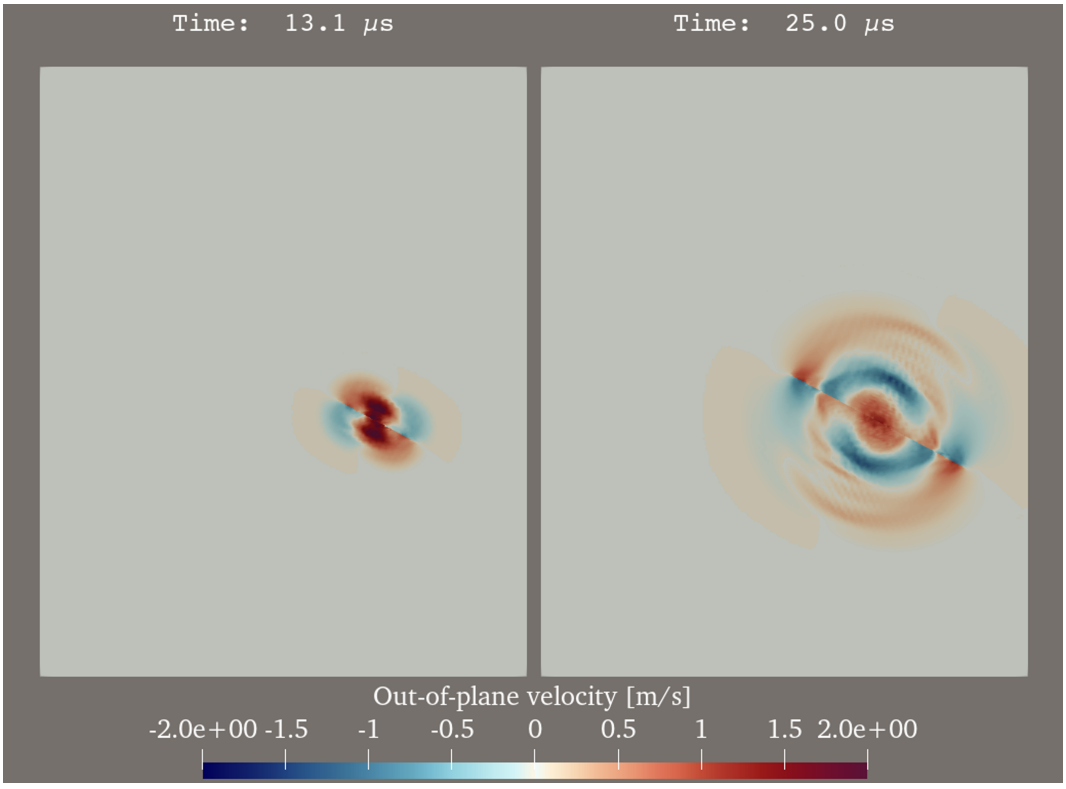


Figure 4.14: Out-of-plane slip field on the interface at two different time instants.



(a)



(b)

Figure 4.15: Out-of-plane velocity field at two different time instants on the front (a) and back (b) of the specimen.

4.6.3 DIC - FE comparison

The best fit with the experimental data is obtained using an interface-normal stress variation $\Delta\sigma$ of 13 MPa, greater than the resolved normal stress $\sigma_0 =$ 12.51 MPa.

For points along the interface with $|x_1| > \frac{D}{2}$ the FE simulation partially represents the experimental data both in terms of slip rate V and interface-parallel velocity $\dot{u}_1$. For example, although the simulated rupture arrives at at almost the same time as in the experiment (16 μs), the slip rate in the FE simulation shows peak values around 8 m/s, while the experimental values reaches values $10 \sim 13$ m/s (Figure 4.16).

On the other hand, for those points that are inside the region where the stress perturbation is imposed ($|x_1| < \frac{D}{2}$) (Figure 4.17a) the FE simulation diverges from experimental data in terms of rupture arrival time which suggests that the strategy adopted to simulate the wire nucleation and other modeling assumptions have a strong impact on the rupture propagation dynamics.

As a matter of fact, In the experiment, the transition from sub-Rayleigh to supershear rupture happens approximatively at 10 mm and 11 µs with the sub-Rayleigh mother crack propagating at 1 m/s and the heading-Supershear at 2.18 m/s. In the simulation, the transition occours at 16 mm and 12 µs. The sub-Rayleigh rupture velocity is slightly higher, 1.2 m/s while, after transition, the supershear rupture speed is 2.16 m/s, very close as the experimental data, as (Figure 4.18).

A first possible reason behind the rupture being faster in the sub-Rayleigh regime could be related to how the stress perturbation is enforced: while in the experiment the wire explosion delivers the information "to deform" the material in a very restricted region of the interface as the wire notch has the size of 0.125 mm, in the code, we impose an instantaneous variation for all

the points over a region that is up to 2 order of magnitude higher, acting as a pre-existing crack. The solution could be to impose a smaller perturbation region D, approximately the size of the wire, and a much greater $\Delta\sigma$.

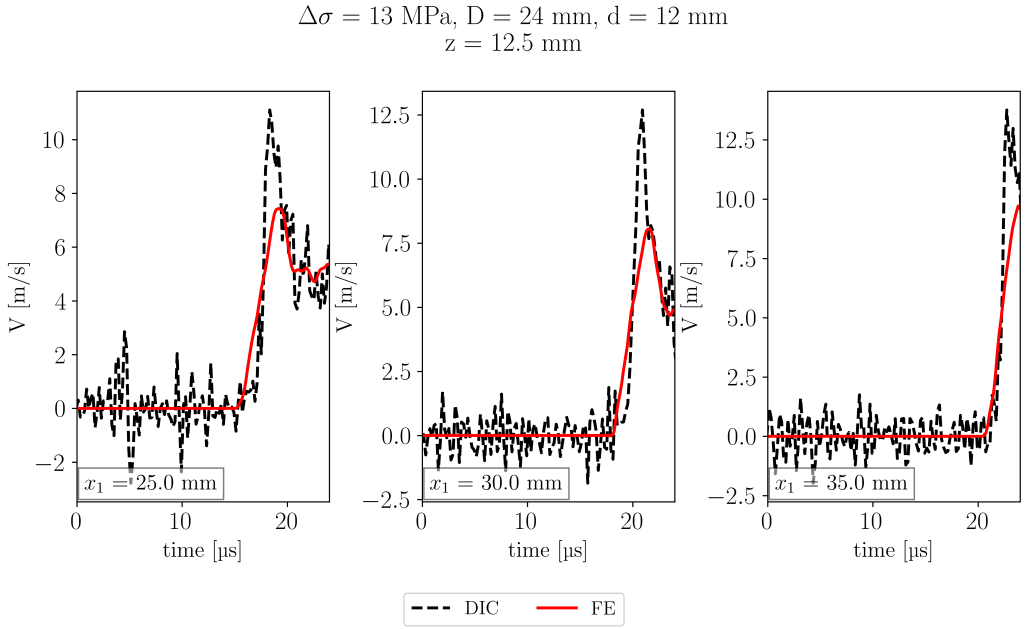
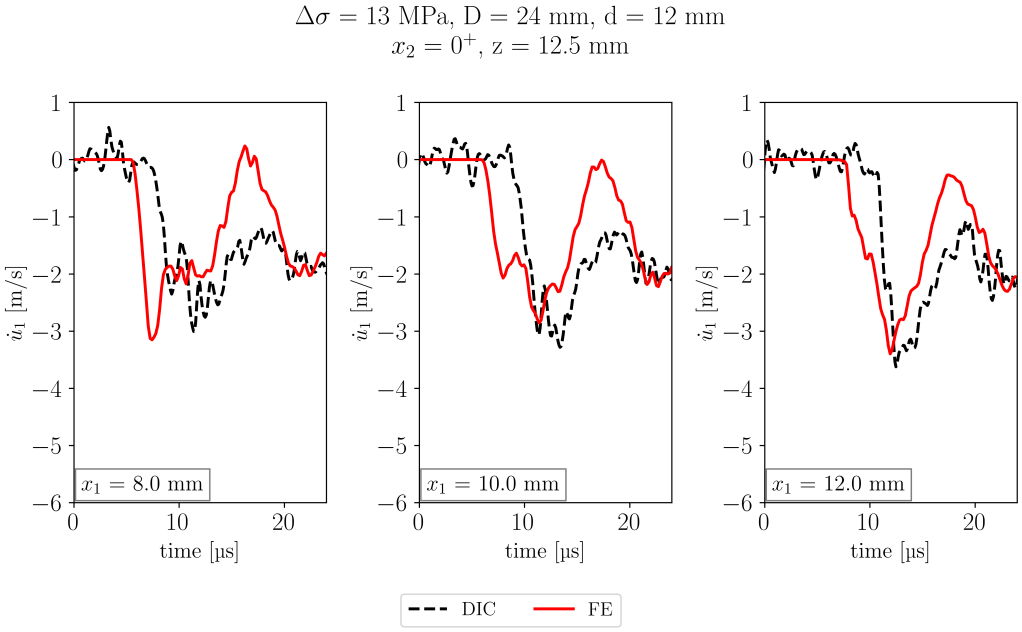
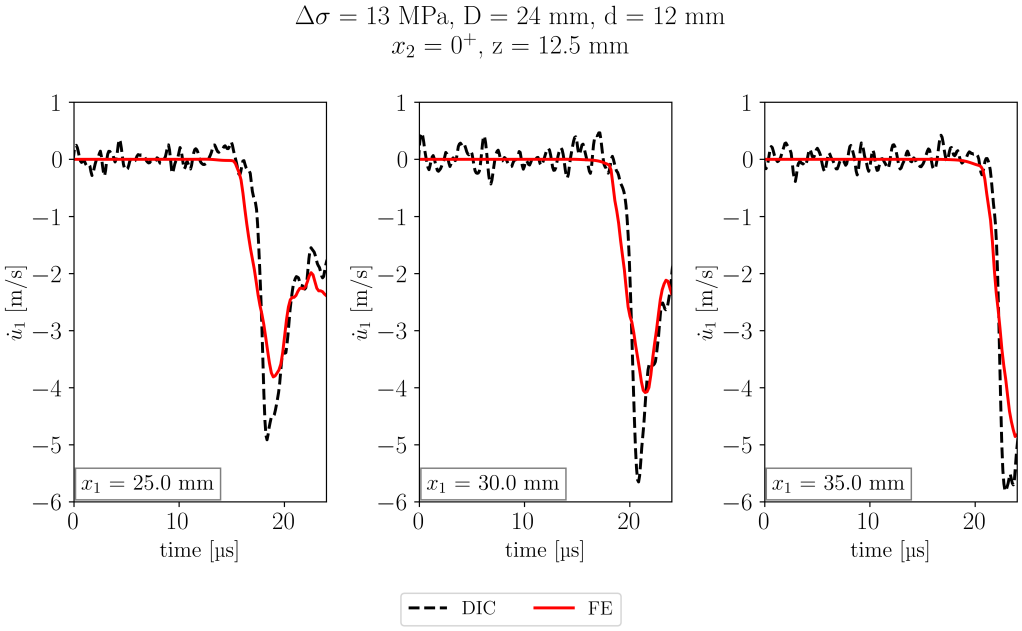


Figure 4.16: Comparison between FE and DIC data of the slip rate at different distances from the nucleation size a



(a)



(b)

Figure 4.17: Interface-parallel velocity at different distances from the nucleation site: $|x_1| \leq D/2$ (a) and $|x_1| > D/2$ (b). FE simulation results are compared with experimental data.

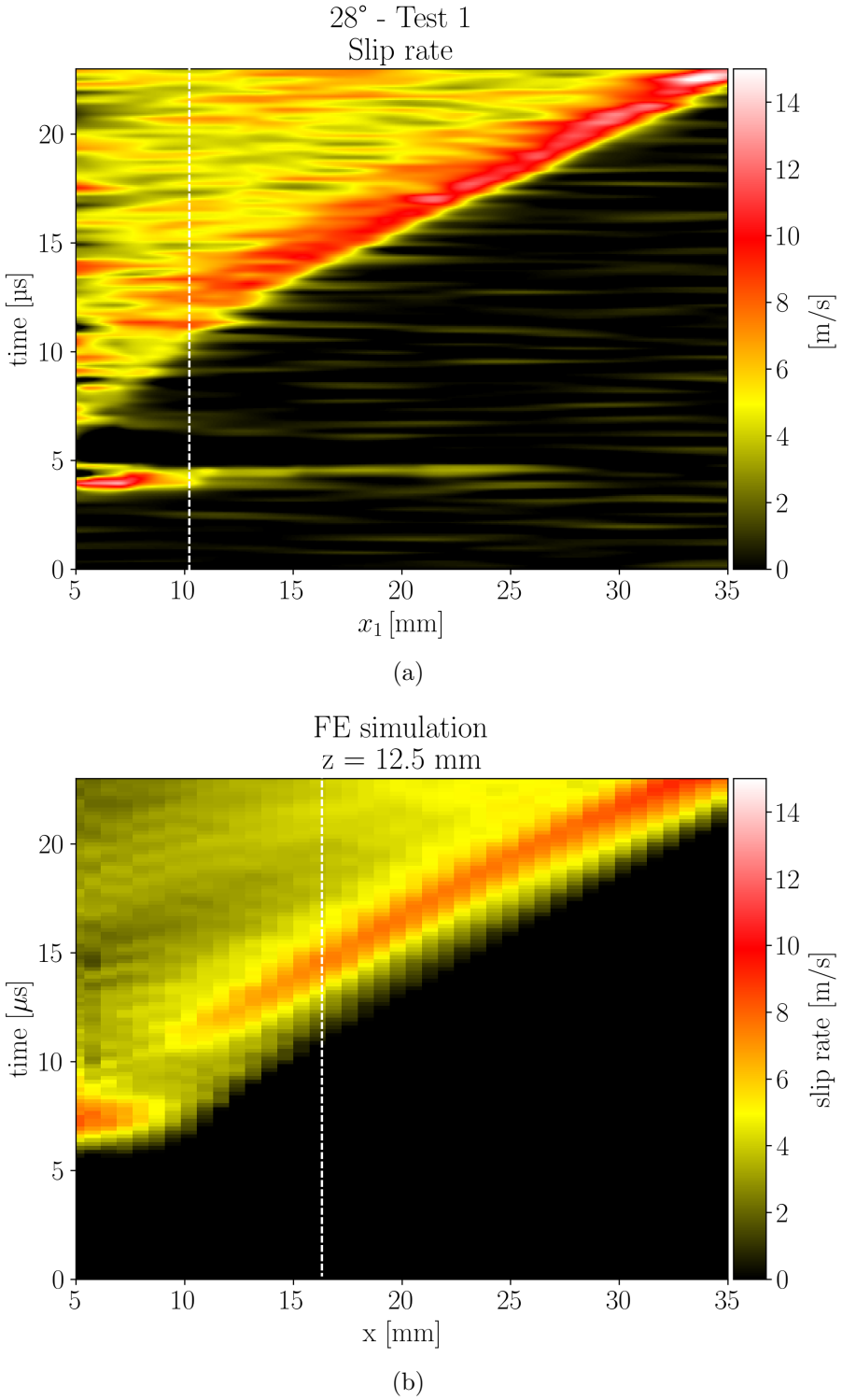


Figure 4.18: Slip rate comparison between experiment (a) and FE simulation (b).

It is worth mentioning that a smaller D allows to simulate the peak in the interface-parallel velocity associated with the P-wave arrival but fails to capture the rupture behaviour as shown in Figure 4.19. This points to the idea that a larger perturbation region does not convey the intense and abrupt stress variation that is localized around the wire notch in the experiments, particularly in the interface-parallel direction. At the same time, for a smaller D, the rupture that is generated propagates at a much lower velocity. Lastly, it should be noted that, in the simulation with $D = 6$ mm, $\Delta\sigma$ is 30 MPa because with $\Delta\sigma = 13$ MPa no rupture would be nucleated.

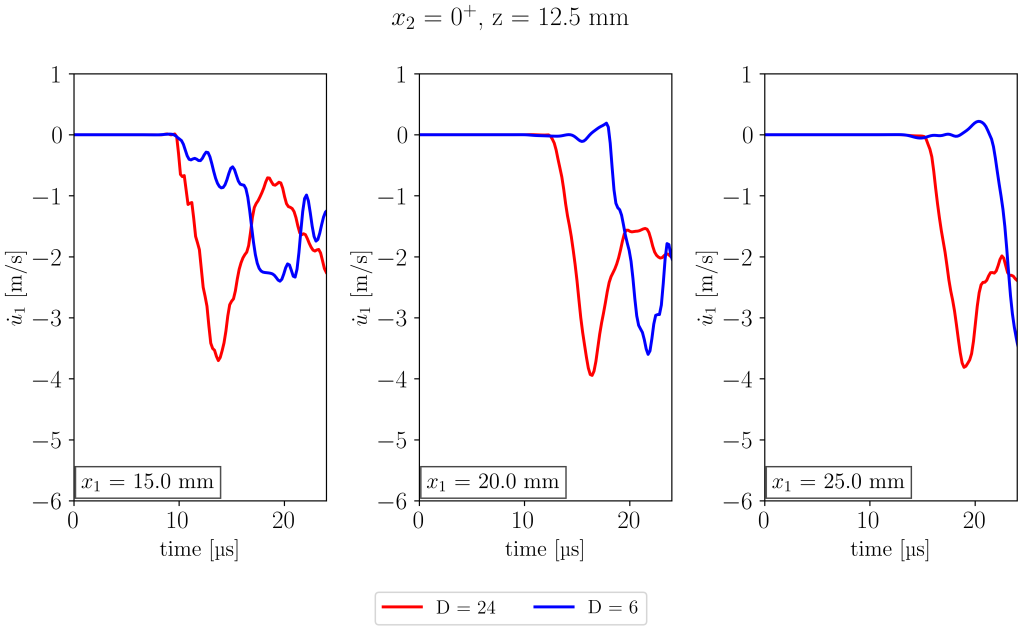
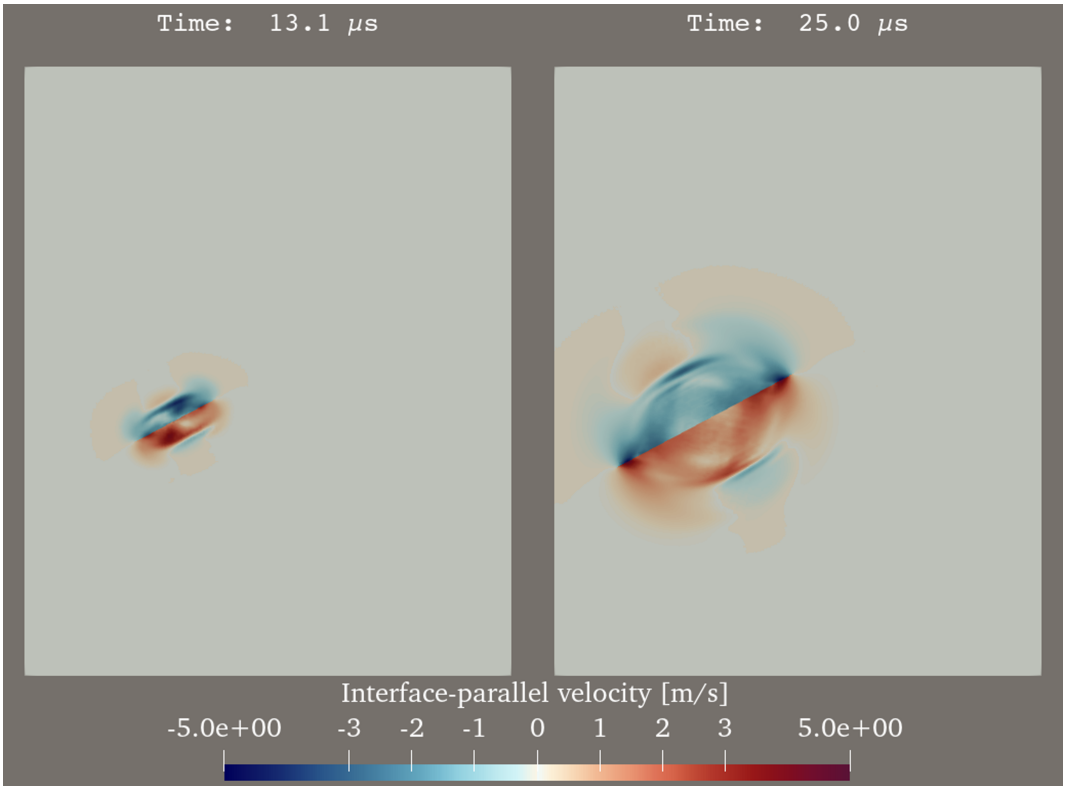


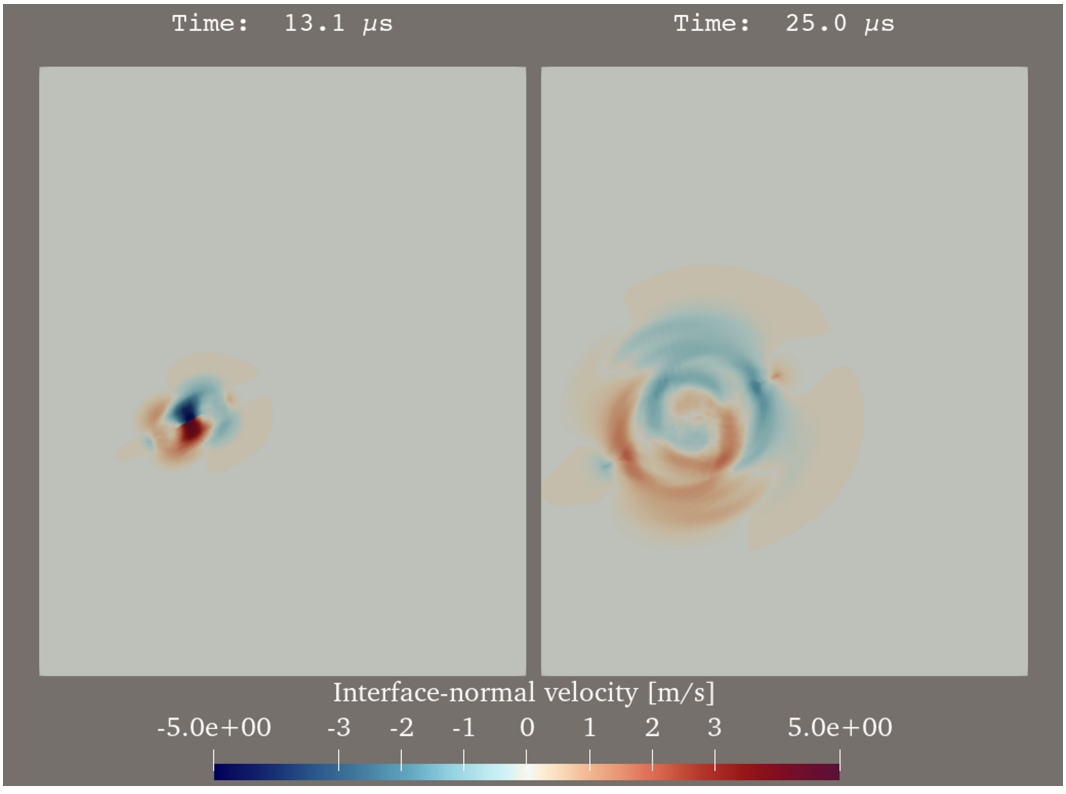
Figure 4.19: Effect of a smaller D on the P-wave velocity peak in the interface-parallel velocity.

While we here discussed only the impact that the nucleation patch has on the rupture propagation properties, one fundamental aspect that has not been considered is the strong effect that the friction modelling has in this phase. We here employed the "aging law" to evolve the state variable, while the "slip-law" has shown to be potentially more suitable to reflects the changes of state-conditions [7], especially when the interface experiences high rate-jumps – here from 10^{-10} m/s to 10^{1} m/s. In fact, the two laws are also characterized by

different D_{RS} that regulates the amount of accumulated slip to steady-state fast sliding. In turn, this affects the initial transient behaviour of the nucleation, most likely altering also the transition point if close to the wire location.



(a)



(b)

Figure 4.20: Interface-parallel (a) and interface-normal (b) velocity field at two different time instants.

Chapter 5

Conclusion

To summarize the results obtained through this work, we can begin by stating that it is possible to trace the dilatational wave generated by the Ni-Cr wire explosion by means of digital image correlation and the measured wave front is coherent with the wave front calculated using the P-wave speed measured with the laser velocimeters. The wave front is stronger on the lower plate where the wire is located and it fades after 12 µs, possibly due to the viscoelastic nature of PMMA. In addition to this, the region affected by the interface-normal stress perturbation is 24 mm and the duration of this perturbation amounts to 4.55 µs. It is difficult to determine the exact stress variation due to the explosion flash affecting the results, but it is clear that there is opening of the interface. Moreover, the stress perturbation is stronger in the lower plate where the Ni-Cr wire is located, which indicates that there is asymmetry.

Furthermore, it can be inferred that the phase following the wire sublimation is independent of both friction and interface angle. Ultimately, the importance of the study of friction to model this type of rupture becomes evident from the profound difference which can be observed when analyzing the rupture from two experiments with different holding time and frictional properties after the nucleation phase and when the rupture starts propagating.

In terms of numerical simulation, the finite element code allows to partially simulate the experiment outside of the region affected by the imposed interface-normal stress perturbation: the supershear rupture velocity is the same as the one obtained from the experiments but the velocity peak is smaller. The transition from sub-Rayleigh to supershear regime happens further away from the nucleation site but roughly at the same time of the experiment because, before transitioning, the sub-Rayleigh rupture velocity is higher than the experimental one; this confirms how the first instants in time are not well represented by an "instantaneous" stress perturbation. In addition, the transition point could also be influenced by the "aging law" used as the state variable evolution law. Ultimately, it is interesting to investigate the out-of-plane velocity field which is associated with the rupture: it emerges that there is out-of-plane slip and the corresponding field is antisymmetrical with respect to the plane perpendicular to the surface containing the nucleation site and the plane parallel to the surface that is located at half the specimen thickness, which is suggests that the out-of-plane slip is caused by the S-waves associated with the rupture.

Concerning future works, while the experimental study might be considered conclusive, from the numerical point of view, it would be noteworthy to explore the effects on the simulation results of a localized stronger stress perturbation as well as a viscoelastic constitutive law.

Bibliography

[1] R. D. Blandford and K. S. Thorne. Applications of classical physics, 2013.

[2] A. J. Rosakis. Intersonic shear cracks and fault ruptures. *Advances in Physics*, 51(4):1189–1257, June 2002.

[3] V. Rubino, A. J. Rosakis, and N. Lapusta. Understanding dynamic friction through spontaneously evolving laboratory earthquakes. *Nature Communications*, 8(1):15991, June 2017.

[4] J. H. Dieterich. Modeling of rock friction: 1. Experimental results and constitutive equations. *Journal of Geophysical Research: Solid Earth*, 84(B5):2161–2168, May 1979.

[5] A. Ruina. Slip instability and state variable friction laws. *Journal of Geophysical Research: Solid Earth*, 88(B12):10359–10370, December 1983.

[6] K. Sirorattanakul. *Response of earthquakes to transient stresses, in laboratory and nature*. PhD thesis, California Institute of Technology, 2024.

[7] P. Bhattacharya, A. M. Rubin, T. E. Tullis, N. M. Beeler, and K. Okazaki. The evolution of rock friction is more sensitive to slip than elapsed time, even at near-zero slip rates. *Proceedings of the National Academy of Sciences*, 119(30):e2119462119, July 2022.

[8] C. H. Scholz. *The Mechanics of Earthquakes and Faulting*. Cambridge University Press, 3 edition, January 2019.

[9] V. Gabuchian. *Experimental Investigation of Thrust Fault Rupture Mechanics*. PhD thesis, California Institute of Technology, 2015.

[10] J. Xu, X. Chen, P. Liu, and Z. Zhang. Ground motion signatures of supershear ruptures in the Burridge-Andrews and free-surface-induced mechanisms. *Tectonophysics*, 791:228570, September 2020.

[11] D. J. Andrews. Rupture velocity of plane strain shear cracks. *Journal of Geophysical Research*, 81(32):5679–5687, November 1976.

[12] K. Xia, A. J. Rosakis, and H. Kanamori. Laboratory Earthquakes: The Sub-Rayleigh-to-Supershear Rupture Transition. *Science*, 303(5665):1859–1861, March 2004.

[13] J.-P. Ampuero and A. M. Rubin. Earthquake nucleation on rate and state faults – Aging and slip laws. *Journal of Geophysical Research: Solid Earth*, 113(B1):2007JB005082, January 2008.

[14] A. M. Rubin and J.-P. Ampuero. Earthquake nucleation on (aging) rate and state faults. *Journal of Geophysical Research: Solid Earth*, 110(B11):2005JB003686, November 2005.

[15] M. Gori, V. Rubino, A. J. Rosakis, and N. Lapusta. Pressure shock fronts formed by ultra-fast shear cracks in viscoelastic materials. *Nature Communications*, 9(1):4754, November 2018.

[16] V. Rubino, A. J. Rosakis, and N. Lapusta. Full-field Ultrahigh-speed Quantification of Dynamic Shear Ruptures Using Digital Image Correlation. *Experimental Mechanics*, 59(5):551–582, June 2019.

[17] V. Rubino, A. J. Rosakis, and N. Lapusta. Spatiotemporal Properties of Sub-Rayleigh and Supershear Ruptures Inferred From Full-Field Dynamic Imaging of Laboratory Experiments. *Journal of Geophysical Research: Solid Earth*, 125(2):e2019JB018922, February 2020.

[18] A. Lattanzi, V. Rubino, M. Rossi, A. Donzelli, A.J. Rosakis, and N. Lapusta. Uncertainty Analysis of Dynamic Rupture Measurements Obtained Through Ultrahigh-Speed Digital Image Correlation. *Experimental Mechanics*, 63(3):529–563, March 2023.

[19] M. Mello, H.S. Bhat, A.J. Rosakis, and H. Kanamori. *Identifying the Unique Ground Motion Signatures of Supershear Earthquakes: Theory and experiments*. PhD thesis, California Institute of Technology, October 2010.

[20] X. Lu. *Combined Experimental and Numerical Study of Spontaneous Dynamic Rupture on Frictional Interfaces*. PhD thesis, California Institute of Technology, 2008.

[21] B. Aagaard, M. Knepley, and C. Williams. *PyLith User Manual*. University of California, Davis, 2019.

[22] S. Liu. *Numerical analyses of frictional sliding on rate-and-state interfaces: Fluid effects, dynamic weakening, and potential-based formulation through machine learning*. PhD thesis, California Institute of Technology, 2024.

[23] P. Dong, R. Chen, K. Xia, W. Yao, Z. Peng, and D. Elsworth. Earthquake Delay and Rupture Velocity in Near-Field Dynamic Triggering Dictated by Stress-Controlled Nucleation. *Seismological Research Letters*, 94(2A):913–924, March 2023.

Acknowledgments

First and foremost, I would like to express my sincerest gratitude to prof. Ares J. Rosakis, for hosting me in his laboratory at the California Institute of Technology. Meeting him has been a privilege and his passion for science and research a great source of inspiration.

I want to sincerely thank dott. Attilio Lattanzi, not only for all the help and support he gave me during the internship, but also for his availability and patience in guiding me through the challenges that accompanied the wonderful experience at Caltech.

I wish to extend my thanks to my advisor prof. Marco Rossi, for his guidance and encouragement throughout the entire process of the internship and thesis preparation.

A special thanks goes to all my university friends. To them, I am grateful for all the days spent together in class, for helping each other in the preparation of exams, and for being a fantastic team in all group projects. They made these years more cheerful and pleasant.

I would like to thank, with all my heart, Alice, Betta, Elena and Giuliana, for always sticking with me and supporting me. With them, I shared countless fears and joys.

A heartfelt thank you goes to my grandparents, Gabriella e Antonio, Rosanna e Aldo. Even if some of them are not with me anymore, each one of my

achievements can also be attributed to their fondness, work and dedication.

I thank Giorgia, for her joyful attitude and her ability to always lift someone's spirit.

There are insufficient words to express the gratitude that I feel for my brother Marco for always being my partner in crime in everything. Growing up together is, day by day, an incredible adventure.

Finally, I want to thank my parents, Monia and Andrea, from the bottom of my heart, for teaching me the importance of love, family, dedication, and perseverance. I thank them for always being great role models and allowing me to chase my dreams.

Ancona, 28 October 2024

Serena Pucci

Ringraziamenti

Vorrei innanzitutto esprimere la mia più sincera gratitudine al prof. Ares J. Rosakis, per avermi ospitato nel suo laboratorio presso il California Institute of Technology. Incontrarlo è stato un privilegio e la sua passione per la ricerca e la scienza è stata una grande fonte di ispirazione.

Desidero esprimere la mia più profonda riconoscenza al dott. Attilio Lattanzi, non solo per tutto l'aiuto, i consigli e il supporto che mi ha offerto nei mesi di tirocinio, ma anche per la sua disponibilià e pazienza nel guidarmi attraverso le sfide che la meravigliosa esperienza a Caltech ha portato con sé.

Ringrazio il mio relatore, il prof. Marco Rossi, per la sua guida e il suo incoraggiamento durante tutta l'esperienza di tirocinio e preparazione della tesi.

Un ringraziamento speciale va a tutti i miei amici dell'università. A loro sono grata per tutte le ore condivise durante le giornate di lezione, per i dubbi chiariti insieme durante le sessioni d'esame e per essere stati un team fantastico in tutti lavori di gruppo. Hanno reso questi anni più leggeri e piacevoli.

Mi piacerebbe ringraziare con tutto il cuore Alice, Betta, Elena e Giuliana, per essermi sempre state accanto e per avermi sempre sostenuto. Essendo loro le persone con cui ho condiviso innumerevoli gioie e paure, posso soltanto aggiungere: «Quando un giorno da un malchiuso portone / tra gli alberi di una corte /ci si mostrano i gialli dei limoni».

Ringraziamenti

Un sentito ringraziamento va ai miei nonni Gabriella e Antonio, Rosanna e Aldo. Anche se alcuni di loro non sono più con me, tutti i risultati che ho raggiunto sono anche merito del loro affetto, lavoro e dedizione.

Ringrazio Giorgia, per la sua gioiosità e capacità di tirare su il morale in ogni situazione.

Non ci sono parole sufficienti per esprimere la gratitudine che provo verso mio fratello Marco, per essere sempre stato il mio complice in tutto. Crescere insieme è di giorno in giorno più bello.

Infine, un grazie dal profondo del cuore ai miei genitori, Monia e Andrea, per avermi insegnato l'importanza dell'amore, della famiglia, della dedizione e della perseveranza, per essere sempre stati un punto di riferimeno e per avermi sempre dato l'opportunità di inseguire i miei sogni.

Ancona, 28 ottobre 2024

Serena Pucci